



KTH ROYAL INSTITUTE
OF TECHNOLOGY

Degree Project in Medical Engineering

Second cycle, 30 credits

Prototype Instrumentation for Frequency Domain fNIRS

KTH Master Thesis

Rohit Rathnam Nareshkumar

Stockholm, Sweden, 2022

Author

Rohit Rathnam Nareshkumar
Medical Engineering
Kungliga Tekniska högskolan

Place for Project

Stockholm, Sweden

Reviewer

Jonas Willén
Kungliga Tekniska högskolan

Supervisor

Rickard Eklöf
Mendi Innovations AB

Examiner

Matilda Larsson
Kungliga Tekniska högskolan

Abstract

Frequency domain fNIRS is a tissue optical measurement technique used to measure absolute haemoglobin concentrations in brain tissue. This work is intended to be the first step in the development of a wearable, low-cost FD-fNIRS device for neurofeedback applications. The system requirements were generated from a review of relevant literature. A simplified system architecture was developed based on the various instrumentation methodologies proposed by various authors. The functional blocks of this system were prototyped and their performance was evaluated. The developed VCSEL current source was found to have a span of 10uA which meets the design specifications. However, challenges exist in optimally biasing SiPM, which is susceptible to optical and electronic noise sources.

Keywords

Neurofeedback, Frequency domain fNIRS, vertical-cavity surface-emitting laser, silicon photomultiplier, vector network analyser

Sammanfattnings

Frekvensdomän fNIRS är en vävnadsoptisk mätteknik som används för att mäta absoluta hemoglobinkoncentrationer i hjärnvävnad. Detta arbete är tänkt att vara det första steget i utvecklingen av en bärbar, en överkomlig kostnad FD-fNIRS-enhet för neurofeedback-applikationer. Systemkraven genererades från en genomgång av relevant litteratur. En förenklad systemarkitektur utvecklades baserat på de olika instrumenteringsmetoderna som föreslagits av olika författare. De funktionella blocken i detta system gjordes prototyper och deras prestanda utvärderades. Den utvecklade VCSEL-strömkällan visade sig ha ett spann på 10uA som uppfyller designspecifikationerna. Det finns dock utmaningar med att optimalt påverka SiPM, som är känsligt för optiska och elektroniska bruskällor.

Nyckelord

Neurofeedback, frekvensdomän fNIRS, laser som utsänder vertikal kavitet, kiselfotomultiplikator, vektornätverksanalysator

Acknowledgements

I am deeply grateful to the talented people at Mendi who gave me the opportunity to be a part of exciting developments at the intersection of brain health and engineering. Special thanks to Rickard Eklöf, CTO and co-founder at Mendi, for his excellent mentorship and guidance throughout this whole process. Many thanks to Dr Mustafa Hamada, Head of Science at Mendi for helping me understand some of the key concepts and relevant literature. I am deeply indebted to Linus Remahl for his instrumental feedback and guidance regarding the hardware design. I would also like to thank my reviewer Jonas Willén and group supervisor Maksims Kornevs for their guidance and feedback in shaping the content of this thesis.

Finally, I would like to express my utmost gratitude to my loving and supportive family, without whom I would not be here.

Stockholm, August 2022

Rohit Rathnam Nareshkumar

Acronyms

AC Alternating Current

APD Avalanche Photodiode

CMOS Complementary Metal Oxide Semiconductor

DAC Digital to Analog Converter

DC Direct Current

EEG Electroencephalography

ERP Event Related Potentials

FD-fNIRS Frequency Domain Functional Near Infrared Spectroscopy

fNIRS Functional Near Infrared Spectroscopy

FPGA Field Programmable Gate Array

LED Light Emitting Diode

MEG Magneto Encephalography

MRI Magnetic Resonance Imaging

NF Neurofeedback

PET Positron Emission Tomography

PIN Positive-Intrinsic-Negative

RF Radio Frequency

SiPM Silicon Photomultiplier

SPECT Single Positron Emission Computed Tomography

VCSEL Vertical-Cavity Surface-Emitting Laser

VNA Vector Network Analyser

List of Figures

2.1.1	Hardware product design process summarised	5
3.1.1	Generalised block diagram	10
3.2.1	Vertical-Cavity Surface-Emitting Laser (VCSEL) response curves . . .	11
3.2.2	Current source with dual-TSV358 configured as an instrumentation amplifier.	12
3.2.3	Digital to Analog Converter (DAC) controlled constant current source simulated in SPICE. Regulated current vs load resistance (left); regulated current vs DAC voltage (right)	13
3.3.1	DC-DC converter layout	13
A.1.1	Early concept sketch	26
A.1.2	Trace impedance calculation	27
A.1.3	Current source output measurement. $1\text{mV} \equiv 1\mu\text{A}$; output variation by $\sim 10\mu\text{A}$	27
A.1.4	AC coupled output from boost converter (5V USB power)	28
A.1.5	AC coupled output from boost converter (3.7V battery power)	28
A.1.6	SiPM output, AC coupled, 5V USB power	29
A.1.7	VCSEL current draw	29
A.1.8	VNA output, 50Ω load	30
A.1.9	Measurement setup	30
A.1.10	Phase 1 schematic diagram	31
A.1.11	Phase 1 PCB front	32
A.1.12	Phase 1 PCB back	32
A.1.13	Phase 2 schematic diagram	33
A.1.14	Phase 2 PCB front	34
A.1.15	Phase 2 PCB back	34

LIST OF FIGURES

B.1.1 Spatial vs Temporal sensitivity in neuroimaging modalities. Adapted from [32]	36
B.2.1 Chromophore absorption coefficients in tissue [34]	37

List of Tables

2.2.1 Minimum operation requirements	6
3.6.1 Table showing the functional status of different subsystems in the design	14
B.3.1 Comparison of different fNIRS techniques [8]	38

Contents

1	Introduction	1
1.1	Aims	2
1.2	Scope	2
1.3	Delimitation	3
1.4	Outline	3
2	Methodology	4
2.1	Hardware Design Process	4
2.2	Frequency Domain Functional Near Infrared Spectroscopy (FD-fNIRS) Instrumentation	5
2.3	Component selection and trade-offs	6
2.3.1	Optical Sources	7
2.3.2	Optical Detectors	7
2.4	Prototype Development Plan	8
3	Results and Discussion	9
3.1	System architecture	9
3.2	VCSEL constant current source	9
3.2.1	Bias calculation	10
3.2.2	SPICE simulation and measured variation	11
3.3	SiPM DC-DC converter	11
3.4	Trace impedance and layout considerations	12
3.5	SiPM output	14
3.6	Summary of Results	14
4	Conclusion and Future Work	15
4.1	Conclusion	15

CONTENTS

4.2 Future work	16
Bibliography	17

Chapter 1

Introduction

The World Health Organization (WHO) defines health as “a state of complete physical, mental and social well-being and not merely the absence of disease or infirmity” [1], recognising the importance of mental health. Unattended mental health has a large detrimental impact on society, with disorders like ADHD estimated to affect approximately 500 million people worldwide [2]. Poor mental health was attributed to have cost the world economy approximately \$2.5 trillion per year in 2010, and this cost is projected to increase to \$6 trillion by 2030 [3]. Although there have been significant advancements in clinically proven pharmacological agents to mitigate the effects of mental health disorders, these solutions do not work favourably for all [3]. A growing body of research suggests neurofeedback training is a viable therapeutic solution to treating mental health disorders [4]. Neurofeedback (NF) training is defined as learning to control brain events by giving sensory and conscious feedback, contingent on the event [5]. It helps in visualising neurophysiological states that the subject is not usually aware of, and helps them to try and regulate it with the aim of improving certain neurocognitive states or alleviating symptoms like auditory verbal hallucinations (schizophrenic patients) and anxiety (patients with social anxiety disorder) [6]. The aim of NF training is to learn to regulate activity in certain brain regions corresponding to known behaviours [7]. Traditional functional neuroimaging aims to establish correlations between neural activity and behaviour mechanisms such as cognition, information processing, and brain changes in the pathological state [8]. Conversely, NF training utilises functional neuroimaging to manipulate neural activity in certain regions corresponding to targeted behaviours. There are various learning models which try to explain closed loop NF training [7]. The enabling technology is

functional neuroimaging which allows for real-time measurement of neural activity. This information is presented to the practitioner enabling them to modify their behaviour patterns. In the past, Electroencephalography (EEG) and functional MRI have been widely utilised to understand neural activation, and behaviour. More recently, Functional Near Infrared Spectroscopy (fNIRS) is gaining traction in NF training [9] which is the focus of this thesis.

1.1 Aims

Essentially, the major aims of this thesis are to:

1. Derive a set of system requirements to build a frequency-domain fNIRS device.
2. Develop the system architecture for a simplified, low-cost proof of concept frequency domain device.
3. Validate the basic functionality of the components and document the challenges and requirements for future work

1.2 Scope

The scope of this work is limited to:

- Performance of a detailed survey of relevant literature pertaining to fNIRS modalities.
- Evaluation of the benefits and drawbacks of the different techniques to implement FD-fNIRS.
- Development of a system architecture for a simplified FD-fNIRS system.
- Generation of a set of requirements for the basic functional blocks constituting a FD-fNIRS device, based on literature.
- Design and fabrication of the basic components of this system.
- Evaluation of the functional blocks in terms of their individual performance.

1.3 Delimitation

Considering the constraints to time and resources, the following delimitation of tasks were imposed. These are deferred to more detailed future work.

- Mechanical assemblies to perform accurate measurements.
- Implementation of an analytical model to extract absorption coefficient μ_a and reduced scattering coefficient μ'_s .
- Calibration and validation of measured optical properties.

1.4 Outline

The rest of this work is divided into three chapters. In the Methodology chapter, the design process has been described. The various FD-fNIRS methodologies from literature have been summarised, with the motivation for different design decisions. The detailed results and implications are discussed in the Results and Discussion chapter respectively. The chapter Conclusion and Future Work summarises the key takeaways from this work, and scope of future developments for the same. The Appendix consists of the background, and additional figures referred to in the text.

Chapter 2

Methodology

In this chapter, the generalised hardware design process is introduced. The cost-benefit analysis performed for selection of components is presented in Section 2.3. Finally, Section 2.4 describes the cyclic development plan undertaken for incremental prototyping.

2.1 Hardware Design Process

The design process for a hardware product begins with the concept development phase. This involves analysis of literature (2.2) and visualisation through concept sketches (Figure A.1.1). The next phase of development is the proof of concept (PoC) or proof of technology (PoT) prototype. The main purpose of the PoC is to demonstrate the underlying concepts behind the product at the lowest possible cost. Once the core functionality is established, the next phase in design is engineering validation testing (EVT). This involves an iterative process of building all of the required features expected of the final product. Design validation testing (DVT) is the subsequent phase, where regulatory requirements and other performance criteria are validated in the design. The final stage is production validation testing (PVT), where the design is optimised for economic scale manufacturability. After this phase, the product is ready for mass production. A summary of the complete design process is shown in Figure 2.1.1. This work is a part of concept development and initial proof of concept phase.

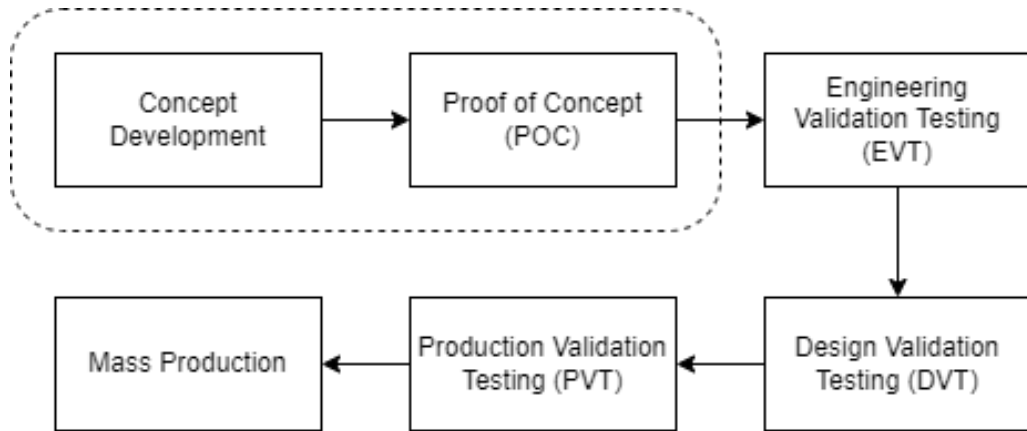


Figure 2.1.1: Hardware product design process summarised

2.2 FD-fNIRS Instrumentation

The core instrumentation needed for FD-fNIRS is optoelectronic circuitry capable of measuring amplitude attenuation and phase delay of a sinusoidal optical signal.

One approach is to use homodyne detection, which is based on in-phase / quadrature (I/Q) demodulator. The system consists of two double-balanced mixers driven by a quadrature reference source. The measured optical signal is multiplied with the source signal and a 90° phase shifted source signal, resulting in I/Q signals. These are low pass filtered to calculate amplitude and phase shift [10–13].

Heterodyne detection in contrast involves downconverting to a lower intermediate frequency. Here the measured optical signal is multiplied with a local oscillator having voltage controlled frequency, to obtain cross correlated signal at an intermediate frequency. A lock-in amplifier is used to extract amplitude and phase information at the intermediate frequency [14–17]. No et al. presented a compact heterodyne based frequency sweep circuit based design [18].

Another approach is to use an RF Vector Network Analyser (VNA) [19, 20] to perform the phase and amplitude measurement. This method involves integrating an off-the-shelf VNA with a laser driver and detector circuit, and is the lowest complexity approach since the majority of the RF signal generation and processing is offloaded to the VNA.

More recent works have reported using digital heterodyning [21] which uses a digital parallel mixer implemented in a field programmable gate array (Field Programmable Gate Array (FPGA)). This approach minimises noise sources resulting from using an

analog mixer.

Zimmerman et al. [22] and Roblyer et al. [23] have reported using direct digital synthesis. This approach uses a high speed DAC to generate arbitrary Radio Frequency (RF) waveforms. On the receiver end, a high speed analog to digital converter digitises the signal, from which attenuation and phase offset are extracted by digital signal processing.

Yun et al. [24] and Sthalekar et al. [25] have reported custom designed Complementary Metal Oxide Semiconductor (CMOS) integrated circuits which implement transimpedance amplifiers to measure sensor current. The amplitude and phase is detected in hardware and output as pulse width modulated signal, which was read out using an FPGA.

From the review of previous works, minimum component specifications are listed in Table 2.2.1

Table 2.2.1: Minimum operation requirements

Module	Property	Value
Optical source	Wavelength	660 / 808 / 850 nm
	Spectral width	<10 nm
	Maximum power	<15 mW
Detector	3dB bandwidth	>800MHz
	Operating wavelength	500 - 1000 nm range
	Minimum optical sensitivity	0.01 mW/cm
Instrumentation	Operating frequency	50 - 500 MHz
	RF power	>2 dBm
	Sensitivity	<-50 dB

2.3 Component selection and trade-offs

Considering the minimal criteria from literature Table 2.2.1, and requirements to keep the cost and complexity low, the VNA approach from Pham et. al [19] was chosen. The following trade-off analysis was done for component selection.

2.3.1 Optical Sources

The optical sources considered include Light Emitting Diode (LED), laser diode and VCSEL. LEDs are the simplest to use optical source - they are cheap and can have simple driving circuitry. They are easily available in a wide range of wavelengths and multi-LED packages, which do not require much consideration regarding power consumption and heat. The biggest drawbacks to using LEDs is their wider spectral width, higher capacitance and rise time. From a survey of parts distributors and major opto electronic manufacturers like Hamamatsu and OSRAM, it was found that the best performing LEDs had a rise time of \sim ns or cutoff frequency of 50MHz [26]. Since our frequency of interest is >50 MHz Laser diodes offer coherent and almost monochromatic light, which can be modulated well into the GHz range. However, they require much more consideration with regards to power source and heating, often requiring the use of bulky optics, heat-sink, and fibre optic cables to carry the light to and from the tissue. This significantly increases cost and complexity. Another drawback is sourcing lasers in the near-infrared range is more expensive. Additional considerations need to be taken in terms of eye safety, which is an important factor when developing a wearable device. VCSELs offer a good trade-off, having the desirable optical properties of a laser diode combined with lower heat and small package of LEDs. Sourcing VCSELs may still be challenging as the available wavelengths are not as widespread as with LEDs or diode lasers. In this work, 15mW VCSEL modules (808/850nm) sourced from Brightlaser Ltd were used.

2.3.2 Optical Detectors

The options considered for optical detectors include Positive-Intrinsic-Negative (PIN) photodiode, Avalanche Photodiode (APD), and APD arrays also known as Silicon Photomultiplier (SiPM). PIN photodiodes are the cheapest and widely available, with a variety of wavelength sensitivity ranges. They however do not have any intrinsic gain, and so require larger die size to capture the required amount of light - this increased die size leads to increased capacitance and therefore makes high frequency operation difficult. The bias voltage required for these is often low. Avalanche photodiodes address this sensitivity versus frequency response dilemma through highly reverse biased diodes, which results in intrinsic gain in the order of 10^3 due to the avalanche effect. However, the reverse bias voltages required to achieve this are upwards of 100V,

which brings some challenges in terms of power and safety in a consumer wearable device. The SiPM is a relatively recent development, consisting of an array of single photon detecting avalanche diodes. They have much higher gain, in the order of 10^6 with bias voltages $\sim 30V$. This gives us an ideal trade-off in terms of higher gain and lower bias voltage requirements. However, the higher gain also results in higher dark current or noise, which has to be dealt with later in the signal chain. The MICRO-RB series SiPM (onsemi) was used in this work.

2.4 Prototype Development Plan

Prototype development was planned as two incremental cycles. Due to challenges in sourcing parts and long lead times caused by the current supply chain crisis and chip shortage, functionally analogous components had to be used in the phase 1 prototype. The phase 1 prototype was designed using a single off-the-shelf 850nm, 20mW VCSEL instead of the required dual wavelength VCSELs from design requirements. The alternative component was in a TO package as shown in Figure A.1.12, which has higher parasitic lead inductance compared to an SMD part, resulting in sub-optimal high frequency performance. The phase 2 prototype was designed, building on lessons learnt from the drawbacks of the phase 1 prototype. The dual SMD package VCSELs were implemented in this phase.

Chapter 3

Results and Discussion

This chapter presents the overall measured outcomes from the phase 1 and 2 prototypes. The relevant implications are discussed at the end of each section. The mathematical modelling undertaken and engineering implementation details are described in Sections 3.2-3.5. Finally, the overall results are summarised in Section 3.6

3.1 System architecture

A simplified system architecture was developed to validate the functionality of the laser driver and sensor as shown in Figure 3.1.1. The two VCSELs are driven using a DAC controlled op amp current source. This bias current is then added to the RF current from the VNA using a bias tee. A boost converter generates the -33V bias voltage to power the SiPM. The output of the SiPM is Alternating Current (AC) coupled to the VNA input port.

3.2 VCSEL constant current source

Since the VCSEL requires a Direct Current (DC) bias to operate, the modulated RF current from the VNA needs to be offset by a DC value. This is accomplished using a bias-tee which combines an RF signal with a DC bias, commonly used to power downstream devices in RF signal chains.

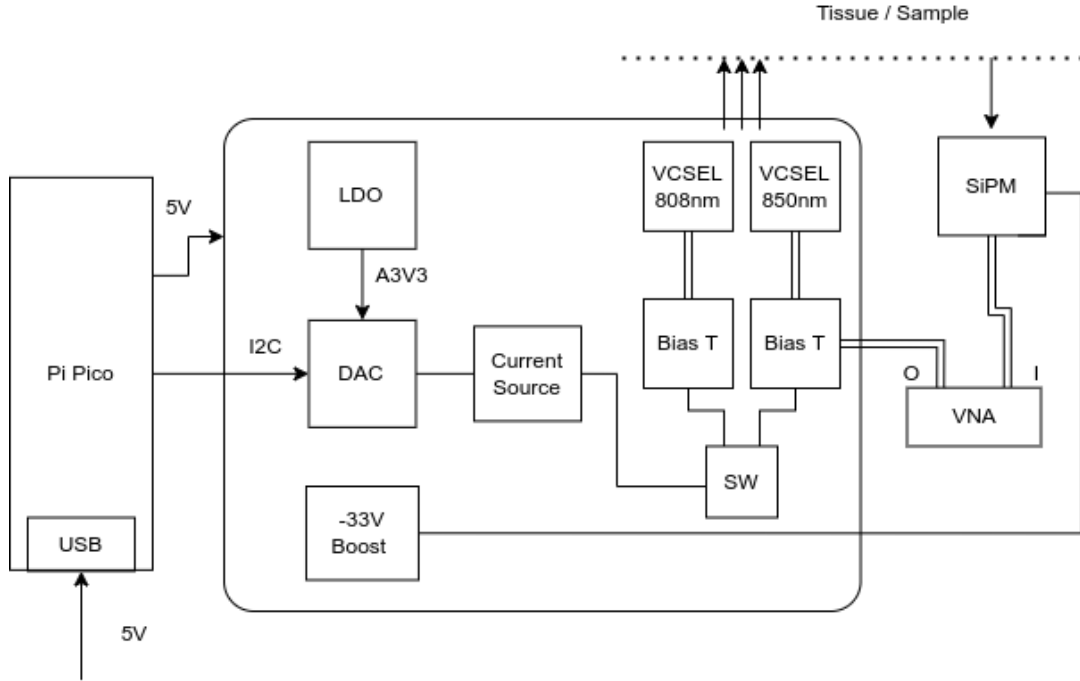


Figure 3.1.1: Generalised block diagram

3.2.1 Bias calculation

In the Figure 3.2.1, the blue trace shows the relationship between current and optical output. The linear response region is seen to be between 1mA to 10mA. An operating point was picked in the middle of this region to prevent skewing of the output sinusoidal waveform. The RF output from the VNA is set at 2dBm which is equivalent to $\pm 0.398\text{V}$. In Figure 3.2.1, the green trace shows the relationship between current and forward voltage, ranging from 1.5 - 2.5V. Since the current requirement is $<20\text{mA}$, a constant current source was designed using op-amps arranged as an instrumentation amplifier [27] as shown in Figure 3.2.2. The complete schematic is shown in Appendix A.1.13. U4A acts as a differential amplifier between the DAC output and the output of U4B, which is a voltage follower on the voltage across load. The output current is given by

$$I_{out} = \frac{V_{in} \times A_v}{R} \quad (3.1)$$

Since the resistors are all matched, the voltage gain $A_v = 1$. Here $R = 10$, and so $I_{out} = V_{DAC}/10$

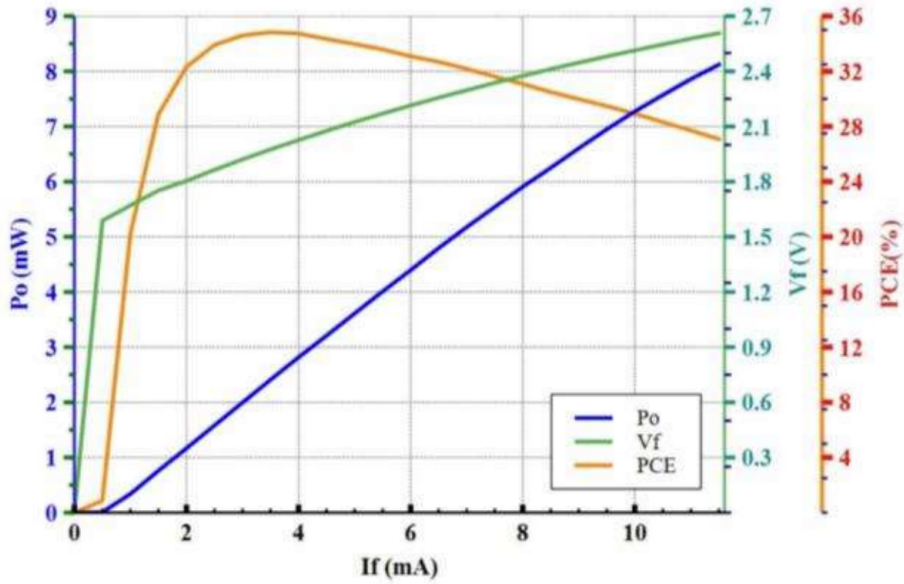


Figure 3.2.1: VCSEL response curves

3.2.2 SPICE simulation and measured variation

Figure 3.2.3 shows the results of SPICE simulation to verify current regulation capability of the circuit. The simulation on the left steps through load impedance (VCSEL impedance) from $40 - 80\Omega$ based on a nominal impedance of 60Ω . Results show current regulation $<1\mu\text{A}$ with 0.1% tolerance resistors. Figure A.1.3 shows the measured variation in constant current output. The output has a span of $\sim 10\mu\text{A}$. The functionality of VCSEL on state by bias voltage was verified through a smartphone camera.

3.3 SiPM DC-DC converter

The SiPM biasing at -33V is accomplished using an inverting DC-DC converter. Figure 3.3.1 shows the layout of boost converter on a 2 layer circuit board. Following guidelines on layout [28], the trace lengths to the inductors, and output decoupling capacitor was kept to a minimum to reduce radiated emissions. A solid ground plane was maintained with minimal breaks to minimise impedance to ground and reduce ground bounce. Figure A.1.4 shows AC coupled measurement of the output from the DC-DC converter. The output has a span of 10mV with some larger spikes in the voltage. Other than the 2.7MHz switching frequency which is expected, a 200kHz noise source was also observed in the output, which saturated the SiPM output (Figure A.1.6).

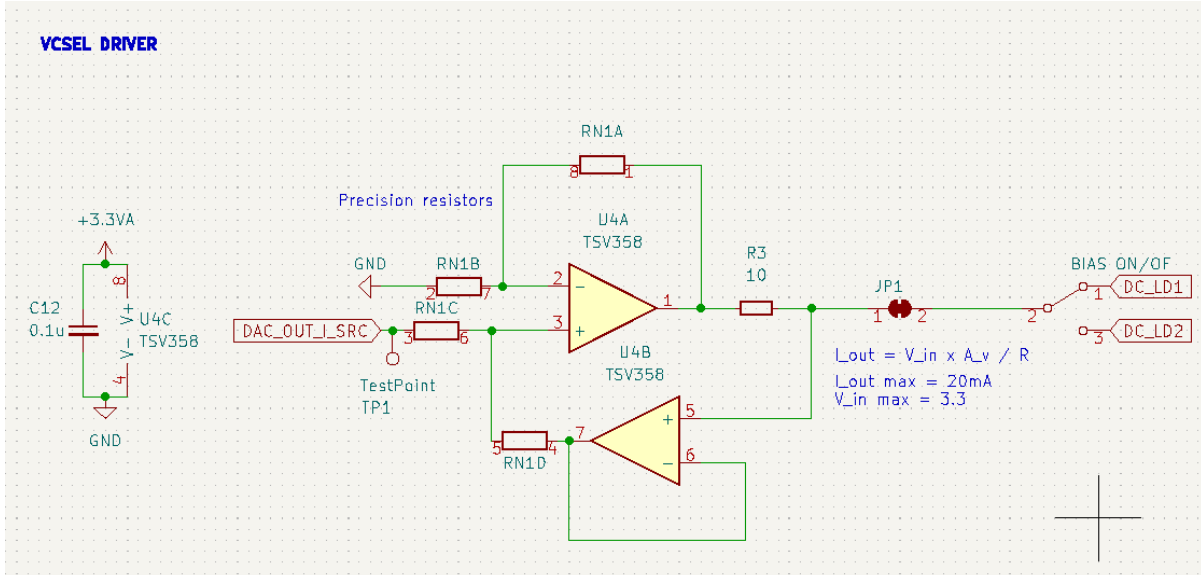


Figure 3.2.2: Current source with dual-TSV358 configured as an instrumentation amplifier.

This noise was suspected to be from the 5V USB power supply, and so it was replaced with a 3.7V lithium polymer battery. Figure A.1.5 shows the output voltage with a battery as the power source. The voltage had an output span <2mV which matches the specification from the manufacturer.

3.4 Trace impedance and layout considerations

Since the VNA works with 50Ω characteristic impedance, the necessary trace width was calculated with KiCAD PCB calculator tool using parameters from the manufacturer. Figure A.1.2 shows the calculated trace width and impedance properties. The characteristic impedance was then measured using the VNA and found to be 48.45Ω . The reflection coefficient Γ is given by

$$\Gamma = \frac{V^-}{V^+} = \frac{Z_{load} - Z_0}{Z_{load} + Z_0} = 10^{-\frac{R_L}{20}} \quad (3.2)$$

where V^+ is the incident wave, V^- is the reflected wave, Z_{load} is the load impedance, and Z_0 is the characteristic impedance. Plugging in the appropriate values, $\Gamma = 0.01574$ and return loss of $36.05dB$. All traces can resonate at odd multiples of $1/4^{th}$ the wavelength of signal passing through them [29]. To mitigate this, ground planes are stitched using vias spaced with $<1/4^{th}$ wavelength apart. The wavelength of the signal can be

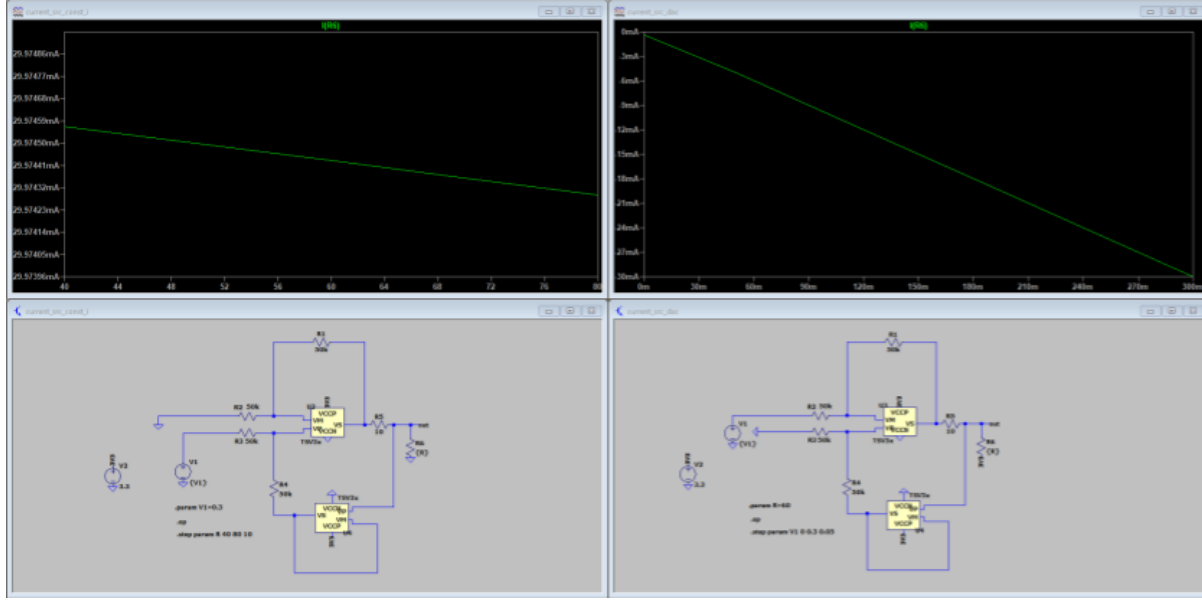


Figure 3.2.3: DAC controlled constant current source simulated in SPICE. Regulated current vs load resistance (left); regulated current vs DAC voltage (right)

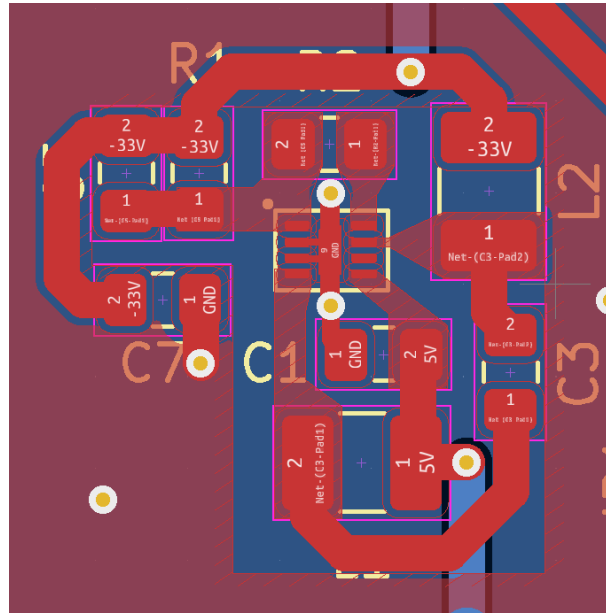


Figure 3.3.1: DC-DC converter layout

calculated by:

$$\lambda = \frac{c}{\sqrt{\epsilon_r}} \frac{1}{\nu} \quad (3.3)$$

where c is the speed of light in vacuum, ϵ_r is the dielectric constant of the PCB substrate, and ν is the frequency of the signal. Substituting the corresponding values, $\lambda = 279.75\text{mm}$. Considering a factor of safety of 3 times, the via spacing set to be below 23mm

3.5 SiPM output

The SiPM response to light was first verified by measuring the DC response to ambient light. The measurement setup was as shown in Figure A.1.9 with the output of the SiPM AC coupled to the oscilloscope. The neutral density filter is used to attenuate the light to prevent SiPM saturation. However, it was not possible to capture a 50MHz test signal produced by the VNA on an oscilloscope. On further investigation of the cause, it was found that the VCSEL drive current waveform does not have the same shape as the VNA output. This can be seen from Figures A.1.7 and A.1.6. A possible cause for this is that the VNA output port could not sufficiently drive the VCSEL. The VNA has a maximum output power level of 2dBm which is ideally 0.398V peak at 50Ω . However, the impedance seen from the port connected to the VNA was measured to be $\sim 120\Omega$, resulting in $\Gamma = 0.583$. This could be due to the input impedance of the VCSEL. The high Γ value indicates that less than half the RF power was being delivered to the VCSEL, resulting in a low modulation depth. One possible solution is to add an RF amplifier to drive the VCSEL rather than directly driving it from the VNA.

3.6 Summary of Results

Table 3.6.1 summarises the results of phase 1 and 2 prototypes. The corresponding schematic and PCB design of both phases are shown in Figure A.1.10-A.1.15. Screen captures of the output measurements from the oscilloscope are shown in Figures A.1.3-A.1.8.

Table 3.6.1: Table showing the functional status of different subsystems in the design

Functionality	Phase 1	Phase 2
Current source	Works, slight deviation in precision resistor footprint	<10 μ A variation
Analog 3.3V rail	Missed enable line in schematic	<80mV variation
Boost converter	Mismatched package footprint	<2mV variation
SiPM bias control	NA	Maximum output limited to -23V, nonlinear potentiometer
VCSEL modulation	NA	Partially works, VNA was unable to direct drive VCSEL

Chapter 4

Conclusion and Future Work

4.1 Conclusion

In conclusion, the VCSEL driver and SiPM bias circuitry were developed, and performed as per specifications. Since the SiPM is a highly sensitive detector, further work is needed to develop a robust enclosure to keep out all light sources. In addition, a precise mechanical assembly is required to align a beam of diameter <1mm with a sensor of dimensions 1mm x 1mm.

Neurofeedback training using fNIRS is a constantly evolving field - although the underlying technology was invented in 1992 [8], it is still accessible only to a few researchers and clinicians. There is a dire need for accessible therapeutic solutions to the mental health problems the world is facing today, and fNIRS could play a key role in it. There exists great potential in democratising this technology and bringing it to the masses in the form of a consumer wearable device. This work shows there are some significant engineering challenges involved in implementing and miniaturising the necessary hardware. The challenges also demonstrated by the fact that there exists only one commercially available FD-fNIRS device by ISS Inc., which is bulky and focused on neuroscience research. Critical recent innovations in RF and photonics, driven by leading edge technology like 5G and LIDAR sensing for autonomous cars, have brought down the technological barriers to developing a viable wearable FD-fNIRS device. Recent work funded by Facebook (Meta) [30] shows there is growing interest from the tech industry, and there is great scope for future developments in this space.

4.2 Future work

The recommendations for possible future work include:

- Design a system for fine control of SiPM bias voltage.
- Implementation of an RF amplifier to control VCSEL modulation depth.
- Construction of a robust mechanical enclosure to keep out external light
- Design and fabrication of a precise alignment mechanism between the VCSEL and SiPM
- Construction of a sample mounting mechanism to perform accurate measurements.
- Online or offline processing of amplitude and phase data to μ_a, μ'_s values. Real-time processing is favourable for neurofeedback applications.
- Calibration of measured optical properties with pre-calibrated tissue phantoms.
- Validation of results against the currently established solutions.

Bibliography

- [1] World Health Organization and Noncommunicable Disease and Mental Health Cluster. *Investing in mental health*. English. OCLC: 1165385474. 2003. ISBN: 9781280097232 9786610097234 9789241562577. URL: <http://www.myilibrary.com?id=9723>.
- [2] Song, Peige, Zha, Mingming, Yang, Qingwen, Zhang, Yan, Li, Xue, and Rudan, Igor. "The prevalence of adult attention-deficit hyperactivity disorder: A global systematic review and meta-analysis". In: *Journal of Global Health* 11 () , p. 04009. ISSN: 2047-2978. DOI: 10.7189/jogh.11.04009. URL: <https://www.ncbi.nlm.nih.gov/pmc/articles/PMC7916320/>.
- [3] Health, The Lancet Global. "Mental health matters". English. In: *The Lancet Global Health* 8.11 (Nov. 2020). Publisher: Elsevier, e1352. ISSN: 2214-109X. DOI: 10.1016/S2214-109X(20)30432-0. URL: [https://www.thelancet.com/journals/langlo/article/PIIS2214-109X\(20\)30432-0/fulltext#articleInformation](https://www.thelancet.com/journals/langlo/article/PIIS2214-109X(20)30432-0/fulltext#articleInformation).
- [4] Enriquez-Geppert, Stefanie, Smit, Diede, Pimenta, Miguel Garcia, and Arns, Martijn. "Neurofeedback as a Treatment Intervention in ADHD: Current Evidence and Practice". en. In: *Current Psychiatry Reports* 21.6 (May 2019), p. 46. ISSN: 1535-1645. DOI: 10.1007/s11920-019-1021-4. URL: <https://doi.org/10.1007/s11920-019-1021-4>.
- [5] Gage, Nicole M. and Baars, Bernard J. "Chapter 8 - Attention and Consciousness". en. In: *Fundamentals of Cognitive Neuroscience (Second Edition)*. Ed. by Nicole M. Gage and Bernard J. Baars. San Diego: Academic Press, Jan. 2018, pp. 247–277. ISBN: 978-0-12-803813-0. DOI: 10.1016/B978-0-12-803813-0.00008-8. URL: <https://www.sciencedirect.com/science/article/pii/B9780128038130000088>.

- [6] Ehliis, Ann-Christine, Barth, Beatrix, Hudak, Justin, Storchak, Helena, Weber, Lydia, Kimmig, Ann-Christin S., Kreifelts, Benjamin, Dresler, Thomas, and Fallgatter, Andreas J. "Near-Infrared Spectroscopy as a New Tool for Neurofeedback Training: Applications in Psychiatry and Methodological Considerations". en. In: *Japanese Psychological Research* 60.4 (2018). _eprint: <https://onlinelibrary.wiley.com/doi/pdf/10.1111/jpr.12225>, pp. 225–241. ISSN: 1468-5884. DOI: 10 . 1111 / jpr . 12225. URL: <https://onlinelibrary.wiley.com/doi/abs/10.1111/jpr.12225>.
- [7] Sitaram, Ranganatha, Ros, Tomas, Stoeckel, Luke, Haller, Sven, Scharnowski, Frank, Lewis-Peacock, Jarrod, Weiskopf, Nikolaus, Blefari, Maria Laura, Rana, Mohit, Oblak, Ethan, Birbaumer, Niels, and Sulzer, James. "Closed-loop brain training: the science of neurofeedback". en. In: *Nature Reviews Neuroscience* 18.2 (Feb. 2017). Number: 2 Publisher: Nature Publishing Group, pp. 86–100. ISSN: 1471-0048. DOI: 10 . 1038/nrn . 2016 . 164. URL: <https://www.nature.com/articles/nrn.2016.164>.
- [8] Ferrari, Marco and Quaresima, Valentina. "A brief review on the history of human functional near-infrared spectroscopy (fNIRS) development and fields of application". eng. In: *NeuroImage* 63.2 (Nov. 2012), pp. 921–935. ISSN: 1095-9572. DOI: 10 . 1016/j.neuroimage . 2012 . 03 . 049.
- [9] Kohl, Simon H., Mehler, David M. A., Lührs, Michael, Thibault, Robert T., Konrad, Kerstin, and Sorger, Bettina. "The Potential of Functional Near-Infrared Spectroscopy-Based Neurofeedback—A Systematic Review and Recommendations for Best Practice". In: *Frontiers in Neuroscience* 14 (2020). ISSN: 1662-453X. URL: <https://www.frontiersin.org/articles/10.3389/fnins.2020.00594>.
- [10] Yang, Yunsong, Liu, Hanli, Li, Xingde, and Chance, Britton. "Low-cost frequency-domain photon migration instrument for tissue spectroscopy, oximetry, and imaging". In: *Optical Engineering* 36.5 (May 1997). Publisher: SPIE, pp. 1562–1569. ISSN: 0091-3286, 1560-2303. DOI: 10 . 1117/1 . 601354. URL: <https://www.spiedigitallibrary.org/journals/optical-engineering/volume-36/issue-5/0000/low-cost-frequency-domain-photon-migration-instrument-for-tissue-spectroscopy/10.1117/1.601354.full>.

- [11] Ramanujam, N., Du, C., Ma, H. Y., and Chance, B. "Sources of phase noise in homodyne and heterodyne phase modulation devices used for tissue oximetry studies". In: *Review of Scientific Instruments* 69.8 (Aug. 1998). Publisher: American Institute of Physics, pp. 3042–3054. ISSN: 0034-6748. DOI: 10.1063/1.1149053. URL: <https://aip.scitation.org/doi/abs/10.1063/1.1149053>.
- [12] Cheung, Cecil, Culver, Joseph P., Takahashi, Kasushi, Greenberg, Joel H., and Yodh, A. G. "In vivocerebrovascular measurement combining diffuse near-infrared absorption and correlation spectroscopies". en. In: *Physics in Medicine and Biology* 46.8 (July 2001). Publisher: IOP Publishing, pp. 2053–2065. ISSN: 0031-9155. DOI: 10.1088/0031-9155/46/8/302. URL: <https://doi.org/10.1088/0031-9155/46/8/302>.
- [13] Yu, Guoqiang, Durduran, Turgut, Furuya, Daisuke, Greenberg, Joel H., and Yodh, Arjun G. "Frequency-domain multiplexing system for in vivo diffuse light measurements of rapid cerebral hemodynamics". EN. In: *Applied Optics* 42.16 (June 2003). Publisher: Optica Publishing Group, pp. 2931–2939. ISSN: 2155-3165. DOI: 10.1364/AO.42.002931. URL: <https://opg.optica.org/ao/abstract.cfm?uri=ao-42-16-2931>.
- [14] Fantini, Sergio, Franceschini, Maria-Angela, Maier, John S., Walker, Scott A., Barbieri, Beniamino B., and Gratton, Enrico. "Frequency-domain multichannel optical detector for noninvasive tissue spectroscopy and oximetry". In: *Optical Engineering* 34.1 (Jan. 1995). Publisher: SPIE, pp. 32–42. ISSN: 0091-3286, 1560-2303. DOI: 10.1117/12.183988. URL: <https://www.spiedigitallibrary.org/journals/optical-engineering/volume-34/issue-1/0000/Frequency-domain-multichannel-optical-detector-for-noninvasive-tissue-spectroscopy-and/10.1117/12.183988.full>.
- [15] McBride, Troy O., Pogue, Brian W., Jiang, Shudong, Österberg, Ulf L., and Paulsen, Keith D. "A parallel-detection frequency-domain near-infrared tomography system for hemoglobin imaging of the breast in vivo". en. In: *Review of Scientific Instruments* 72.3 (2001), p. 1817. ISSN: 00346748. DOI: 10.1063/1.1344180. URL: <http://scitation.aip.org/content/aip/journal/rsi/72/3/10.1063/1.1344180>.

- [16] Nissilä, Ilkka, Kotilahti, Kalle, Fallström, Kim, and Katila, Toivo. “Instrumentation for the accurate measurement of phase and amplitude in optical tomography”. In: *Review of Scientific Instruments* 73.9 (Sept. 2002). Publisher: American Institute of Physics, pp. 3306–3312. ISSN: 0034-6748. DOI: 10.1063/1.1497496. URL: <https://aip.scitation.org/doi/abs/10.1063/1.1497496>.
- [17] Nissilä, Ilkka, Noponen, Tommi, Kotilahti, Kalle, Katila, Toivo, Lipiäinen, Lauri, Tarvainen, Tanja, Schweiger, Martin, and Arridge, Simon. “Instrumentation and calibration methods for the multichannel measurement of phase and amplitude in optical tomography”. In: *Review of Scientific Instruments* 76.4 (Apr. 2005). Publisher: American Institute of Physics, p. 044302. ISSN: 0034-6748. DOI: 10.1063/1.1884193. URL: <https://aip.scitation.org/doi/abs/10.1063/1.1884193>.
- [18] No, Keun Sik and Chou, P.H. “Mini-FDPM and heterodyne mini-FDPM: handheld non-invasive breast cancer detectors based on frequency-domain photon migration”. In: *IEEE Transactions on Circuits and Systems I: Regular Papers* 52.12 (Dec. 2005). Conference Name: IEEE Transactions on Circuits and Systems I: Regular Papers, pp. 2672–2685. ISSN: 1558-0806. DOI: 10.1109/TCSI.2005.857927.
- [19] Pham, Tuan H., Coquoz, Olivier, Fishkin, Joshua B., Anderson, Eric, and Tromberg, Bruce J. “Broad bandwidth frequency domain instrument for quantitative tissue optical spectroscopy”. In: *Review of Scientific Instruments* 71.6 (June 2000). Publisher: American Institute of Physics, pp. 2500–2513. ISSN: 0034-6748. DOI: 10.1063/1.1150665. URL: <https://aip.scitation.org/doi/10.1063/1.1150665>.
- [20] Gultekin Gulsen, Bin Xiong, Ozlem Birgul, and Orhan Nalcioglu. *Design and implementation of a multifrequency near-infrared diffuse optical tomography system*. URL: <https://www.spiedigitallibrary.org/journals/journal-of-biomedical-optics/volume-11/issue-1/014020/Design-and-implementation-of-a-multifrequency-near-infrared-diffuse-optical/10.1117/1.2161199.full>.
- [21] Arnesano, Cosimo, Santoro, Ylenia, and Gratton, Enrico. “Digital parallel frequency-domain spectroscopy for tissue imaging”. In: *Journal of Biomedical*

- Optics* 17.9 (Sept. 2012). Publisher: SPIE, p. 096014. ISSN: 1083-3668, 1560-2281. DOI: 10 . 1117 / 1 . JBO . 17 . 9 . 096014. URL: <https://www.spiedigitallibrary.org/journals/journal-of-biomedical-optics/volume-17/issue-9/096014/Digital-parallel-frequency-domain-spectroscopy-for-tissue-imaging/10.1117/1.JBO.17.9.096014.full>.
- [22] Zimmermann, Bernhard B., Fang, Qianqian, Boas, David A., and Carp, Stefan A. "Frequency domain near-infrared multiwavelength imager design using high-speed, direct analog-to-digital conversion". In: *Journal of Biomedical Optics* 21.1 (Jan. 2016). Publisher: SPIE, p. 016010. ISSN: 1083-3668, 1560-2281. DOI: 10.1117/1.JBO.21.1.016010. URL: <https://www.spiedigitallibrary.org/journals/journal-of-biomedical-optics/volume-21/issue-1/016010/Frequency-domain-near-infrared-multiwavelength-imager-design-using-high-speed/10.1117/1.JBO.21.1.016010.full>.
- [23] Roblyer, Darren, O'Sullivan, Thomas D., Warren, Robert V., and Tromberg, Bruce J. "Feasibility of direct digital sampling for diffuse optical frequency domain spectroscopy in tissue". en. In: *Measurement Science and Technology* 24.4 (Mar. 2013). Publisher: IOP Publishing, p. 045501. ISSN: 0957-0233. DOI: 10.1088/0957-0233/24/4/045501. URL: <https://doi.org/10.1088/0957-0233/24/4/045501>.
- [24] Yun, Ruida and Koomson, Valencia Joyner. "A Novel CMOS Frequency-Mixing Transimpedance Amplifier for Frequency Domain Near Infrared Spectroscopy". In: *IEEE Transactions on Circuits and Systems I: Regular Papers* 60.1 (Jan. 2013). Conference Name: IEEE Transactions on Circuits and Systems I: Regular Papers, pp. 84–94. ISSN: 1558-0806. DOI: 10.1109/TCSI.2012.2215701.
- [25] Sthalekar, Chirag Chaitanya and Koomson, Valencia Joyner. "A CMOS Sensor for Measurement of Cerebral Optical Coefficients Using Non-Invasive Frequency Domain Near Infrared Spectroscopy". In: *IEEE Sensors Journal* 13.9 (Sept. 2013). Conference Name: IEEE Sensors Journal, pp. 3166–3174. ISSN: 1558-1748. DOI: 10.1109/JSEN.2013.2260651.
- [26] *High-speed switching of IR-LEDs - Background and data sheet definition.* Tech. rep. AN096. OSRAM Opto Semiconductors, 2018.
- [27] Wong, James. *Analog Devices AN-106*. URL: <https://www.analog.com/media/en/technical-documentation/application-notes/28080533AN106.pdf>.

BIBLIOGRAPHY

- [28] *Five Steps to a Good PCB Layout of a Boost Converter*. May 2016. URL: https://www.ti.com/lit/an/slva773/slva773.pdf?ts=1660094478722&ref_url=https%253A%252F%252Fwww.google.com%252F.
- [29] Hageman, Steve. *Via spacing on high-performance PCBs*. en-US. Feb. 2013. URL: <https://www.edn.com/via-spacing-on-high-performance-pcbs/>.
- [30] Wathen, Jeremiah J., Fitch, Michael J., Pagán, Vincent R., Milsap, Griffin W., McDowell, Emil G., Spietz, Lafe, Markow, Zachary E., Trobaugh, Jason W., Richter, Edward J., Eggebrecht, Adam T., Culver, Joseph P., Blodgett, David W., and Hendrickson, Scott M. “A 32-channel frequency-domain fNIRS system based on silicon photomultiplier receivers”. In: *Optical Techniques in Neurosurgery, Neurophotonics, and Optogenetics*. Vol. 11629. SPIE, Mar. 2021, pp. 62–79. DOI: 10.1117/12.2581482. URL: <https://www-spiedigitallibrary-org.focus.lib.kth.se/conference-proceedings-of-spie/11629/116291P/A-32-channel-frequency-domain-fNIRS-system-based-on-silicon/10.1117/12.2581482.full>.
- [31] Roy, Rubén, Vega, Rocío de la, Jensen, Mark P., and Miró, Jordi. “Neurofeedback for Pain Management: A Systematic Review”. In: *Frontiers in Neuroscience* 14 (2020). ISSN: 1662-453X. URL: <https://www.frontiersin.org/article/10.3389/fnins.2020.00671>.
- [32] Strangman, Gary, Boas, David A, and Sutton, Jeffrey P. “Non-invasive neuroimaging using near-infrared light”. en. In: *Biological Psychiatry* 52.7 (Oct. 2002), pp. 679–693. ISSN: 0006-3223. DOI: 10.1016/S0006-3223(02)01550-0. URL: <https://www.sciencedirect.com/science/article/pii/S0006322302015500>.
- [33] Kocsis, L., Herman, P., and Eke, A. “The modified Beer-Lambert law revisited”. eng. In: *Physics in Medicine and Biology* 51.5 (Mar. 2006), N91–98. ISSN: 0031-9155. DOI: 10.1088/0031-9155/51/5/N02.
- [34] Kamrani, Ehsan. “On-chip integrated functional near infra-red spectroscopy (fNIRS) photoreceiver for portable brain imaging”. PhD thesis. Jan. 2014.
- [35] Wilcox, Teresa and Biondi, Marisa. “fNIRS in the developmental sciences”. en. In: *WIREs Cognitive Science* 6.3 (2015). _eprint: <https://onlinelibrary.wiley.com/doi/pdf/10.1002/wcs.1343>, pp. 263–

BIBLIOGRAPHY

283. ISSN: 1939-5086. DOI: 10 . 1002 / wcs . 1343. URL: <https://onlinelibrary.wiley.com/doi/abs/10.1002/wcs.1343>.
- [36] Althobaiti, Murad and Al-Naib, Ibraheem. “Recent Developments in Instrumentation of Functional Near-Infrared Spectroscopy Systems”. en. In: *Applied Sciences* 10.18 (Jan. 2020). Number: 18 Publisher: Multidisciplinary Digital Publishing Institute, p. 6522. DOI: 10.3390/app10186522. URL: <https://www.mdpi.com/2076-3417/10/18/6522>.
- [37] Liebert, Adam, Wabnitz, Heidrun, Steinbrink, Jens, Obrig, Hellmuth, Möller, Michael, Macdonald, Rainer, Villringer, Arno, and Rinneberg, Herbert. “Time-resolved multidistance near-infrared spectroscopy of the adult head: intracerebral and extracerebral absorption changes from moments of distribution of times of flight of photons”. EN. In: *Applied Optics* 43.15 (May 2004). Publisher: Optica Publishing Group, pp. 3037–3047. ISSN: 2155-3165. DOI: 10.1364/AO.43.003037. URL: <https://opg.optica.org/ao/abstract.cfm?uri=ao-43-15-3037>.
- [38] Fantini, Sergio and Sassaroli, Angelo. “Frequency-Domain Techniques for Cerebral and Functional Near-Infrared Spectroscopy”. In: *Frontiers in Neuroscience* 14 (2020), p. 300. ISSN: 1662-453X. DOI: 10.3389/fnins.2020.00300. URL: <https://www.frontiersin.org/article/10.3389/fnins.2020.00300>.
- [39] Haskell, Richard C., Svaasand, Lars O., Tsay, Tsong-Tseh, Feng, Ti-Chen, McAdams, Matthew S., and Tromberg, Bruce J. “Boundary conditions for the diffusion equation in radiative transfer”. EN. In: *JOSA A* 11.10 (Oct. 1994). Publisher: Optical Society of America, pp. 2727–2741. ISSN: 1520-8532. DOI: 10.1364/JOSAA.11.002727. URL: <https://www.osapublishing.org/josaa/abstract.cfm?uri=josaa-11-10-2727>.
- [40] Wray, Susan, Cope, Mark, Delpy, David T., Wyatt, John S., and Reynolds, E. Osmund R. “Characterization of the near infrared absorption spectra of cytochrome aa₃ and haemoglobin for the non-invasive monitoring of cerebral oxygenation”. en. In: *Biochimica et Biophysica Acta (BBA) - Bioenergetics* 933.1 (Mar. 1988), pp. 184–192. ISSN: 0005-2728. DOI: 10.1016/0005-2728(88)90069-2. URL: <https://www.sciencedirect.com/science/article/pii/0005272888900692>.

BIBLIOGRAPHY

- [41] *Optical Absorption of Hemoglobin.* URL: [https://omlc.org/spectra/hemoglobin/.](https://omlc.org/spectra/hemoglobin/)

Appendix - Contents

A Additional Figures	26
A.1 Appendix	26
B Background	35
B.1 Imaging modalities for neurofeedback training	35
B.2 Mechanism of fNIRS	36
B.3 fNIRS techniques	37
B.4 Analytical Model	38

Appendix A

Additional Figures

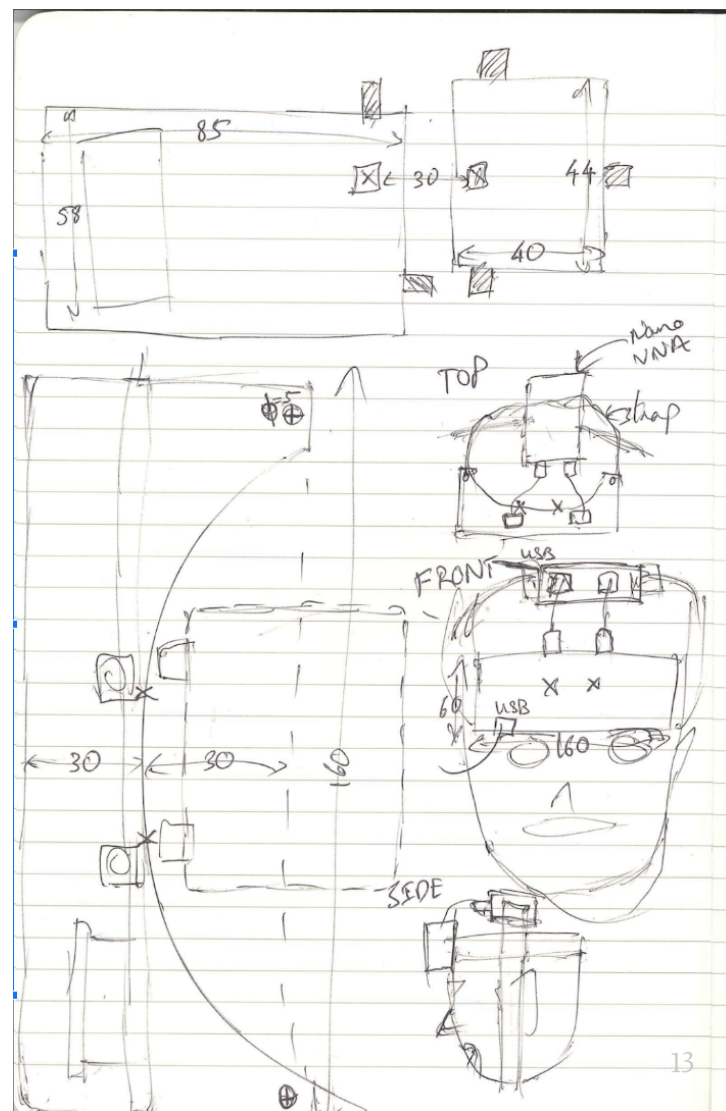


Figure A.1.1: Early concept sketch

APPENDIX A. ADDITIONAL FIGURES

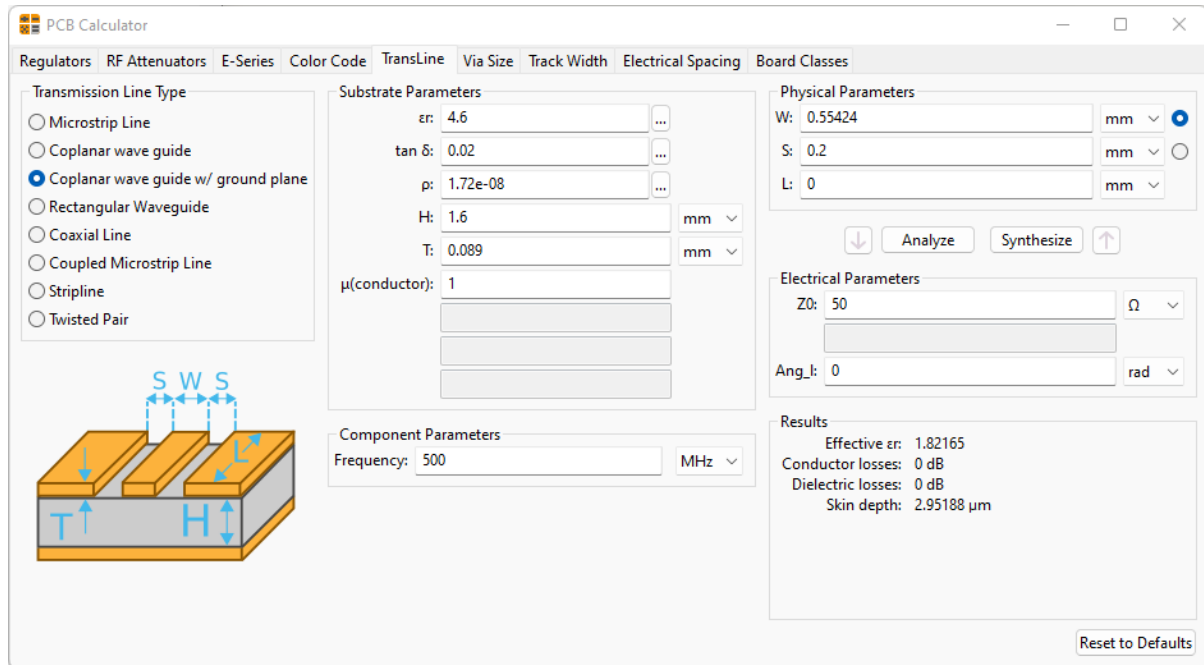


Figure A.1.2: Trace impedance calculation

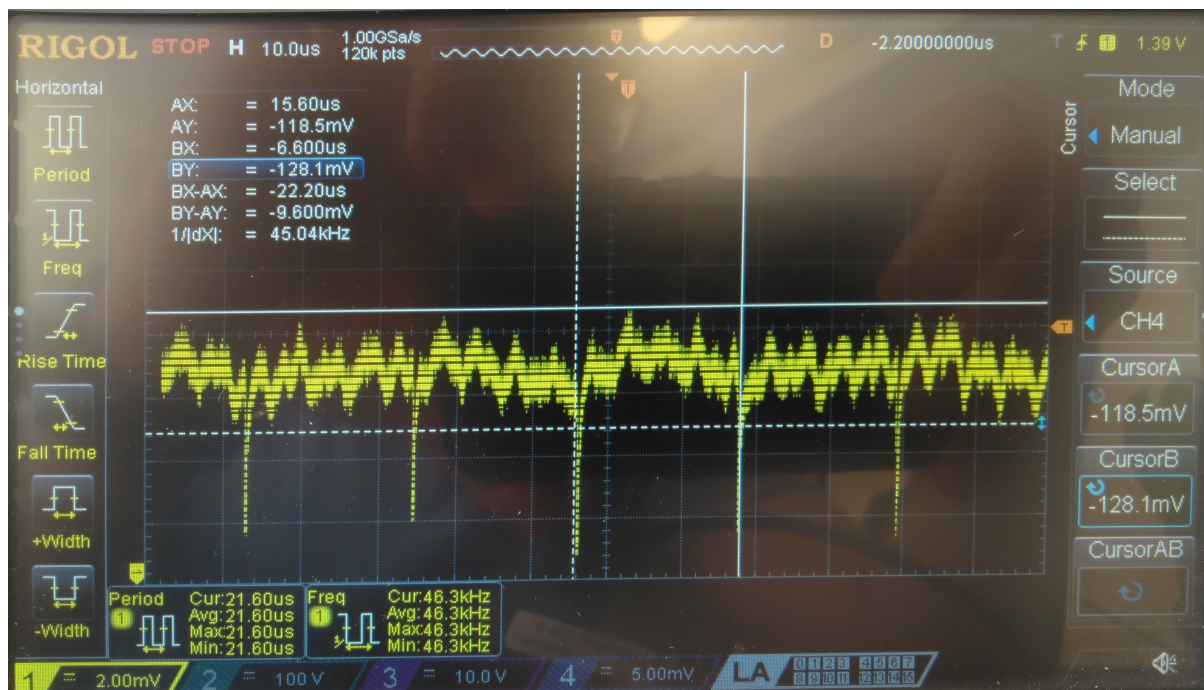


Figure A.1.3: Current source output measurement. 1mV \equiv 1uA; output variation by \sim 10uA

APPENDIX A. ADDITIONAL FIGURES

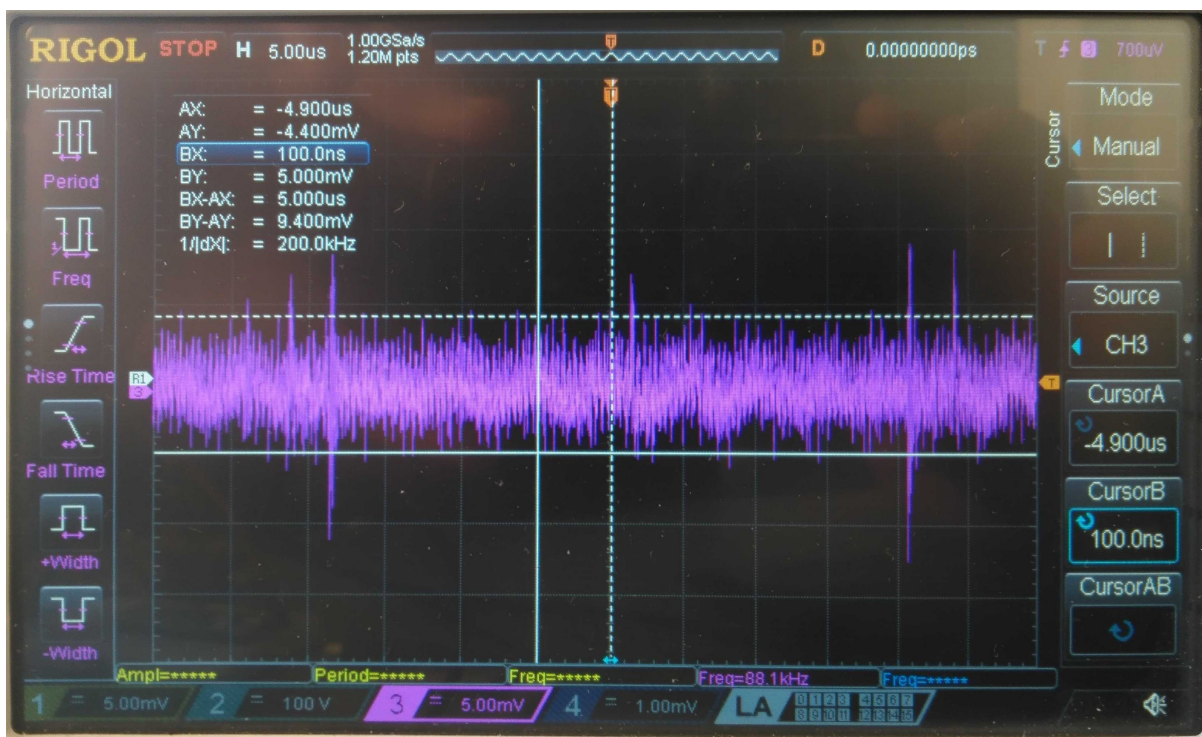


Figure A.1.4: AC coupled output from boost converter (5V USB power)

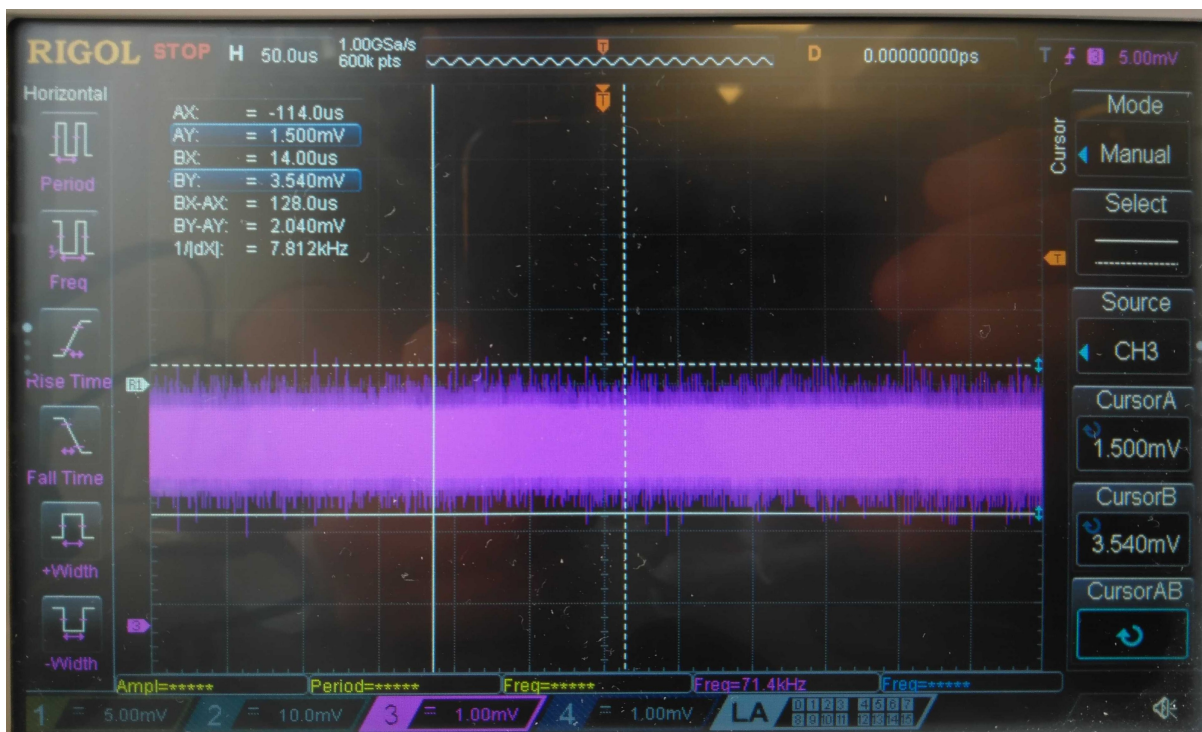


Figure A.1.5: AC coupled output from boost converter (3.7V battery power)

APPENDIX A. ADDITIONAL FIGURES

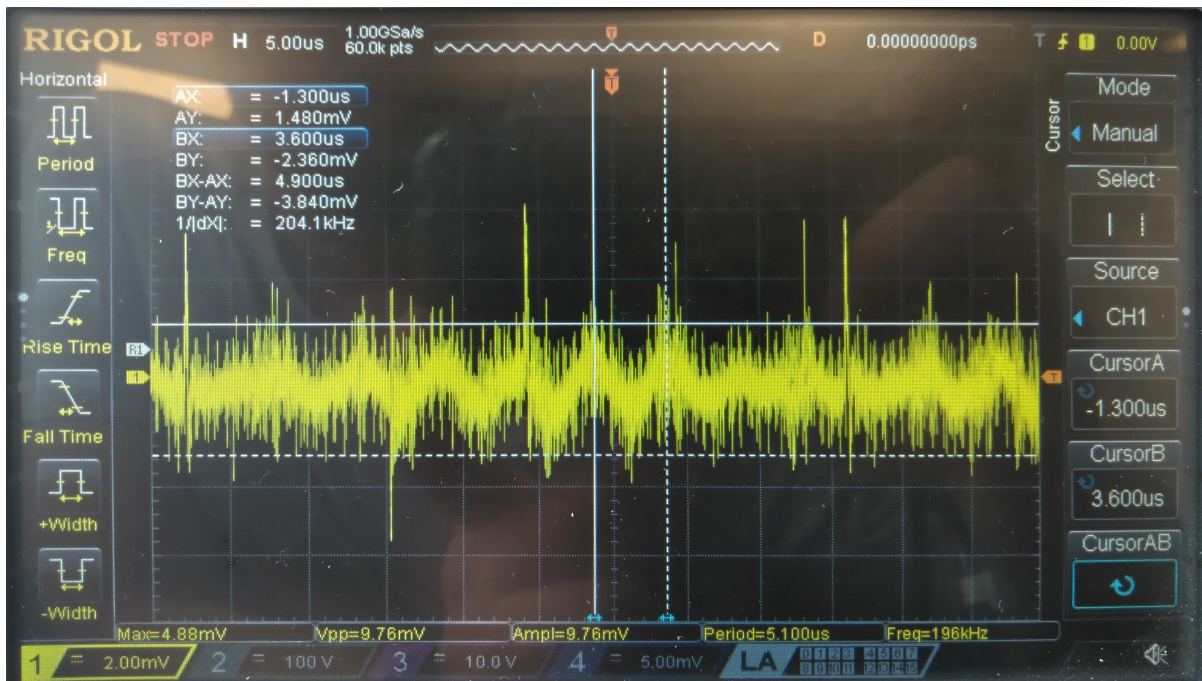


Figure A.1.6: SiPM output, AC coupled, 5V USB power

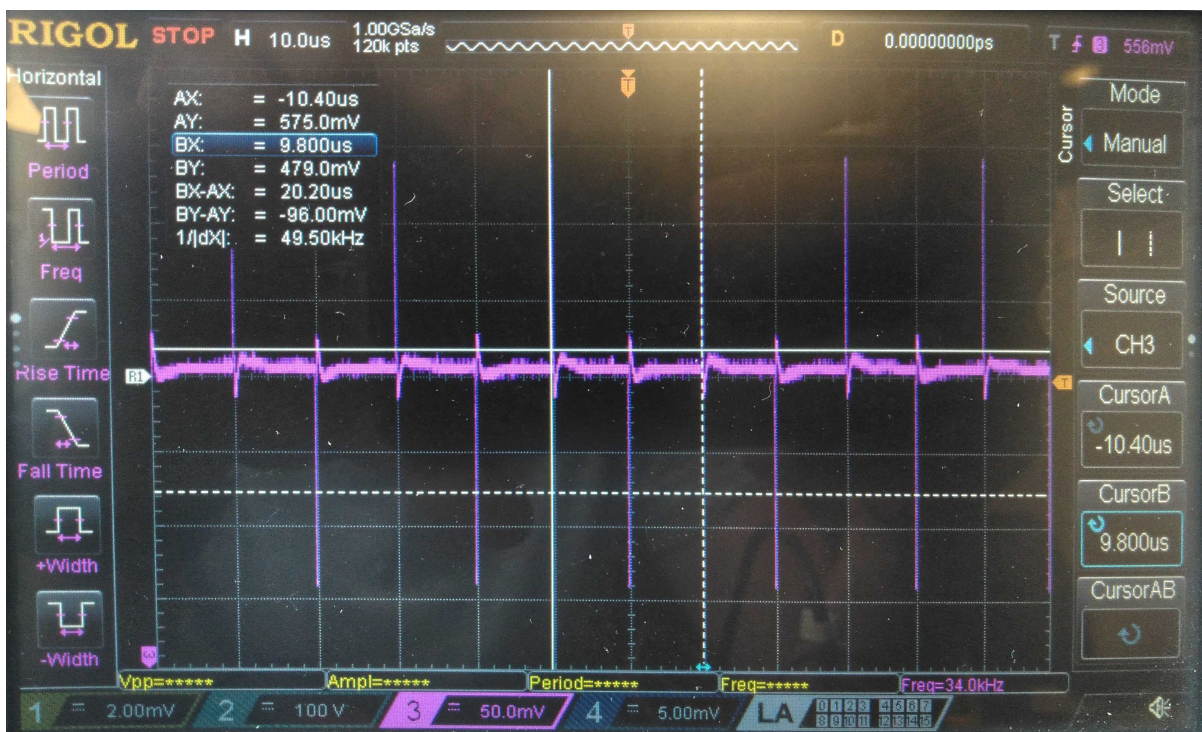


Figure A.1.7: VCSEL current draw

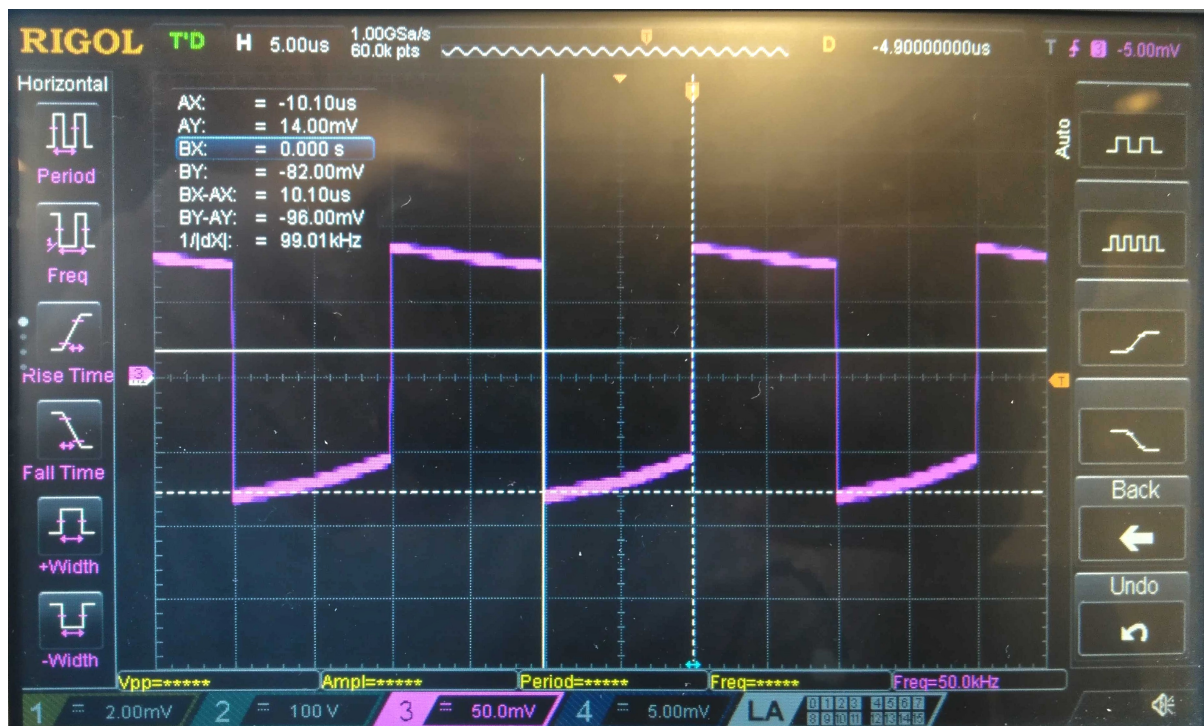


Figure A.1.8: VNA output, 50Ω load

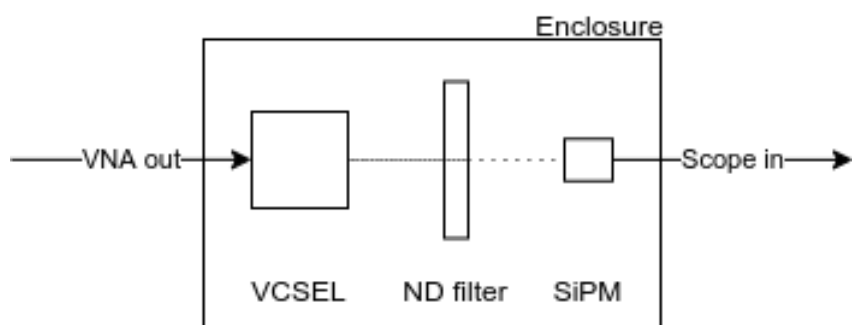


Figure A.1.9: Measurement setup

APPENDIX A. ADDITIONAL FIGURES

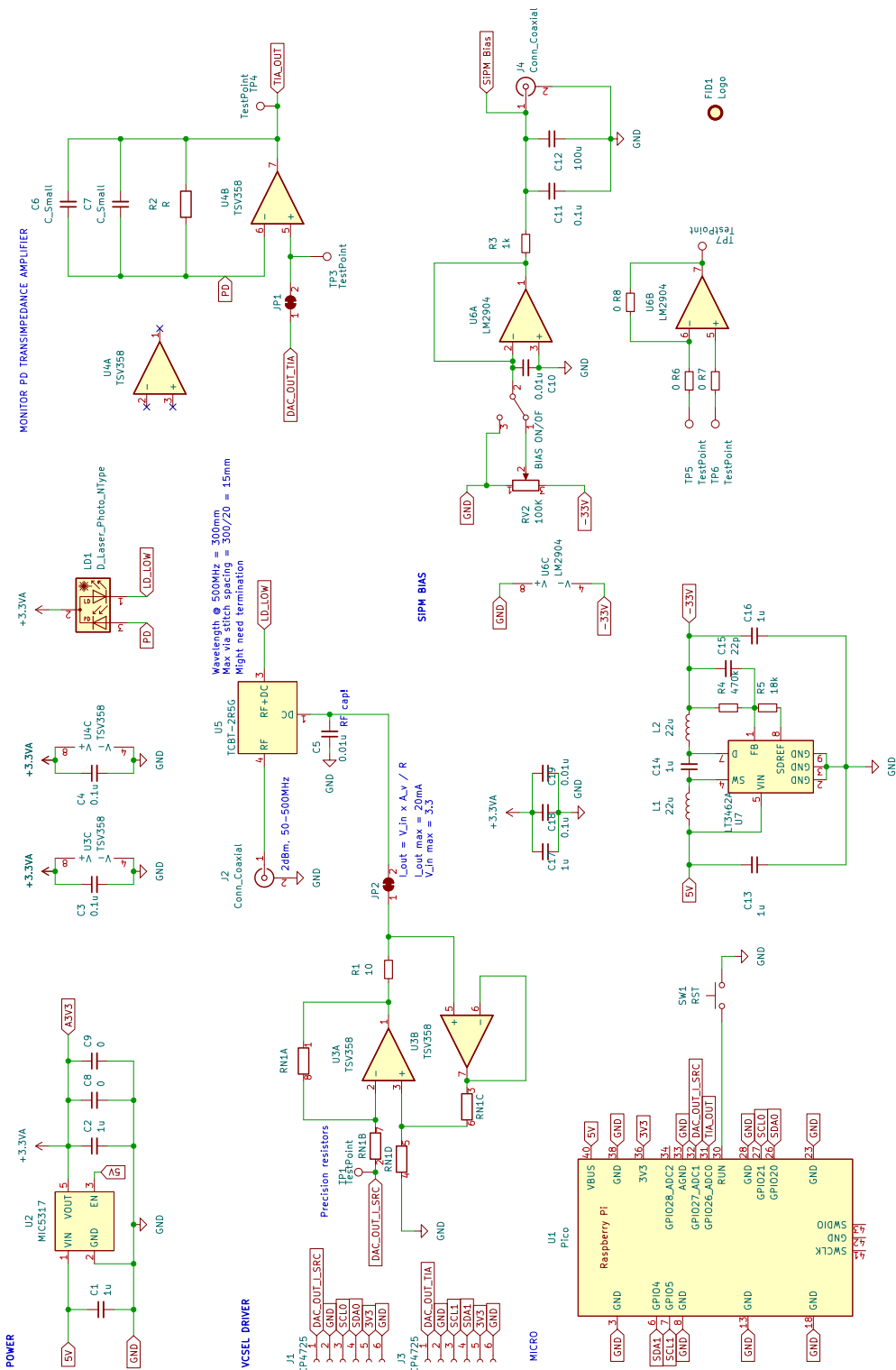


Figure A.1.10: Phase 1 schematic diagram

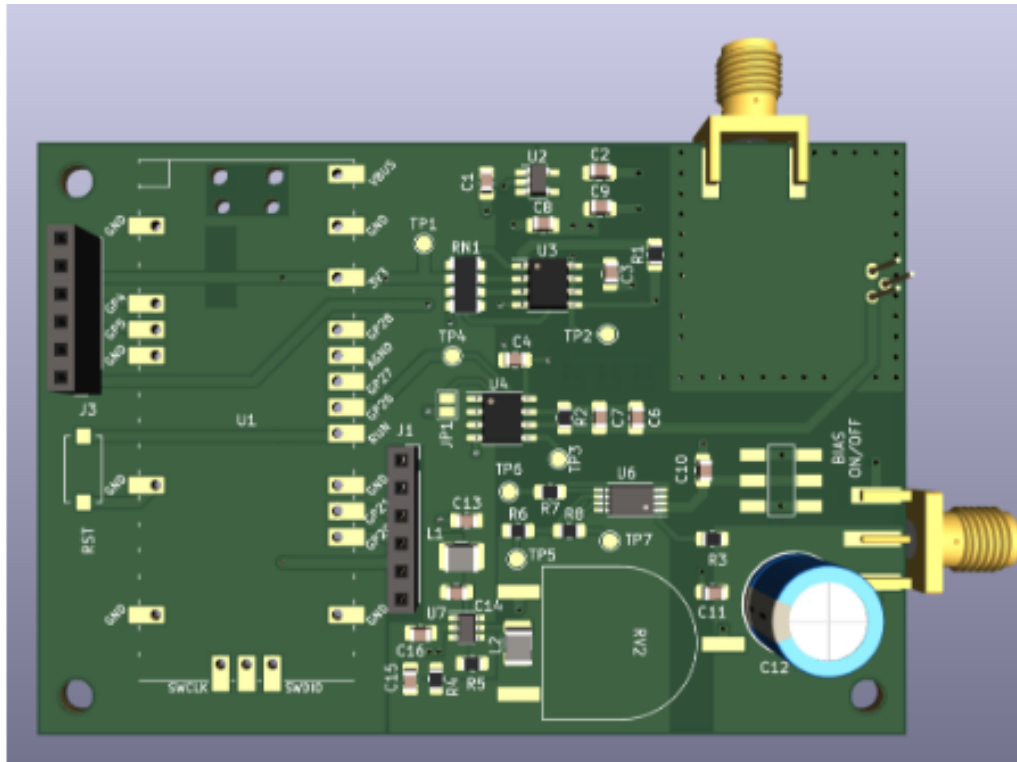


Figure A.1.11: Phase 1 PCB front

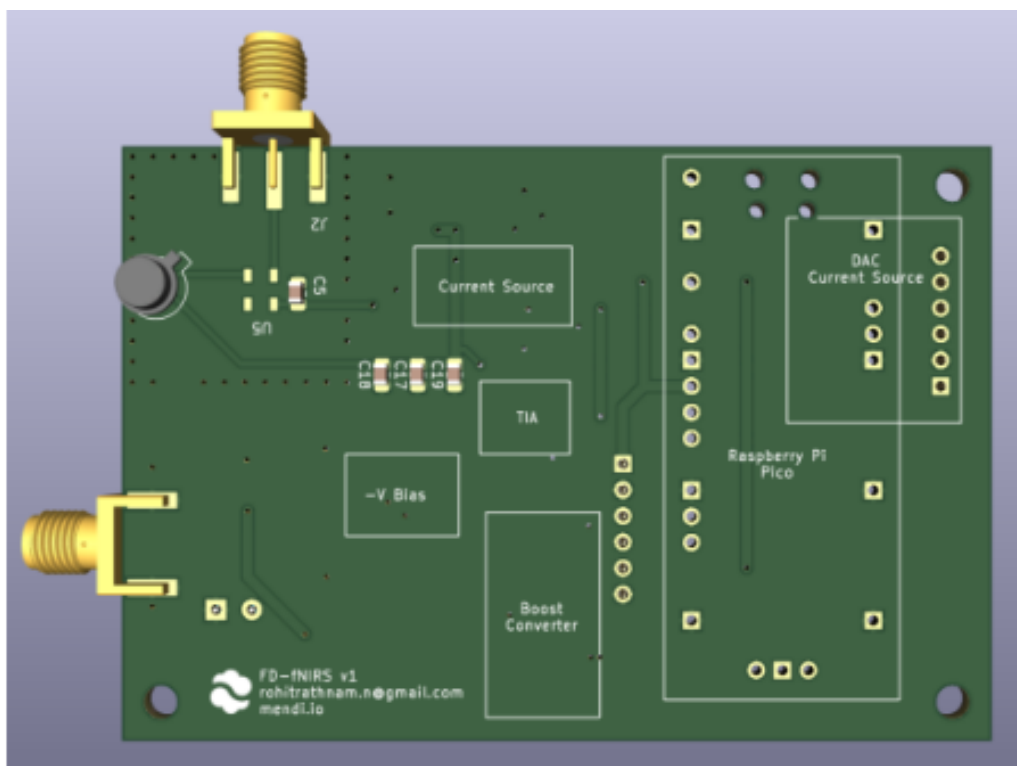


Figure A.1.12: Phase 1 PCB back

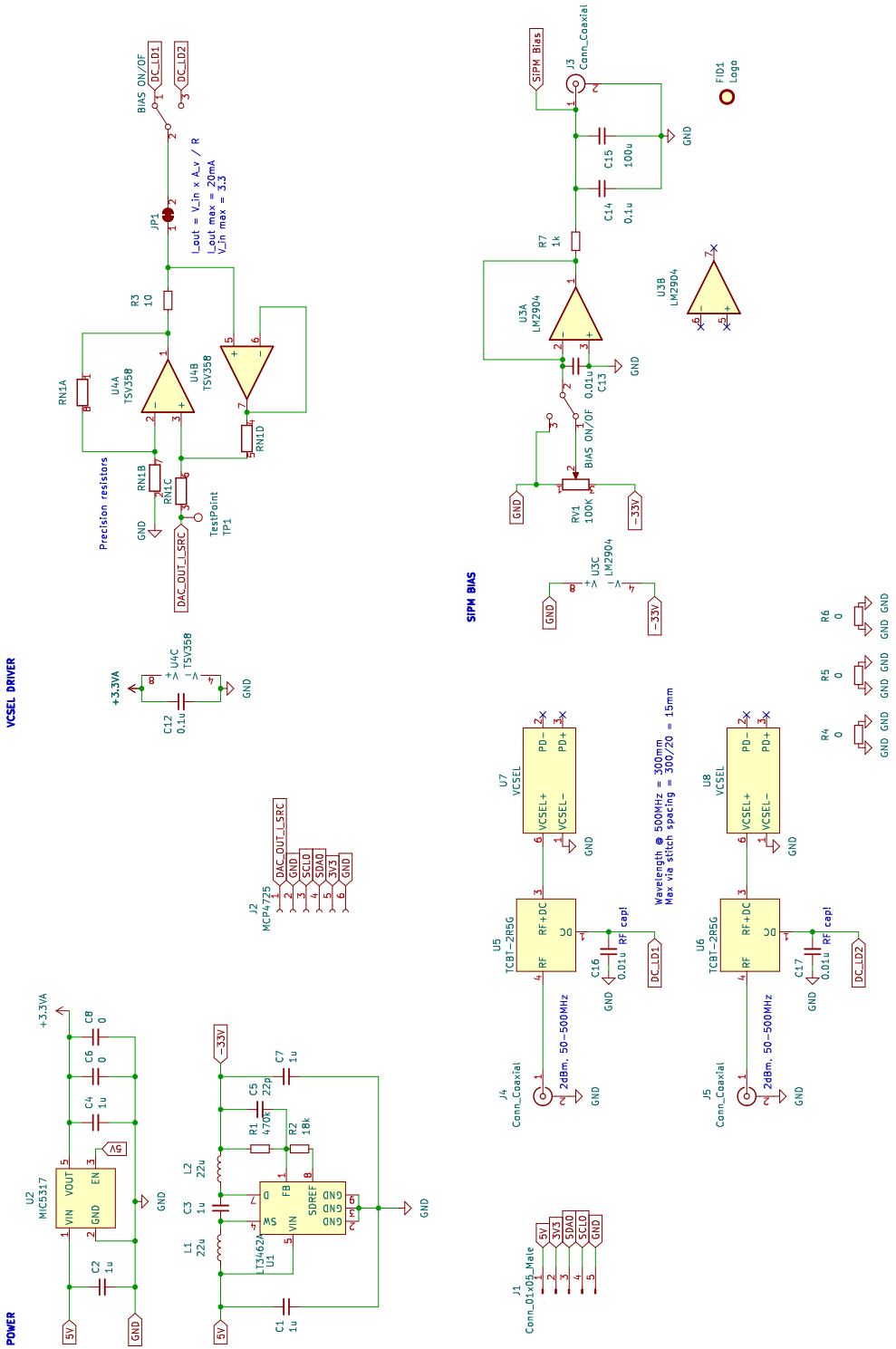


Figure A.1.13: Phase 2 schematic diagram

APPENDIX A. ADDITIONAL FIGURES

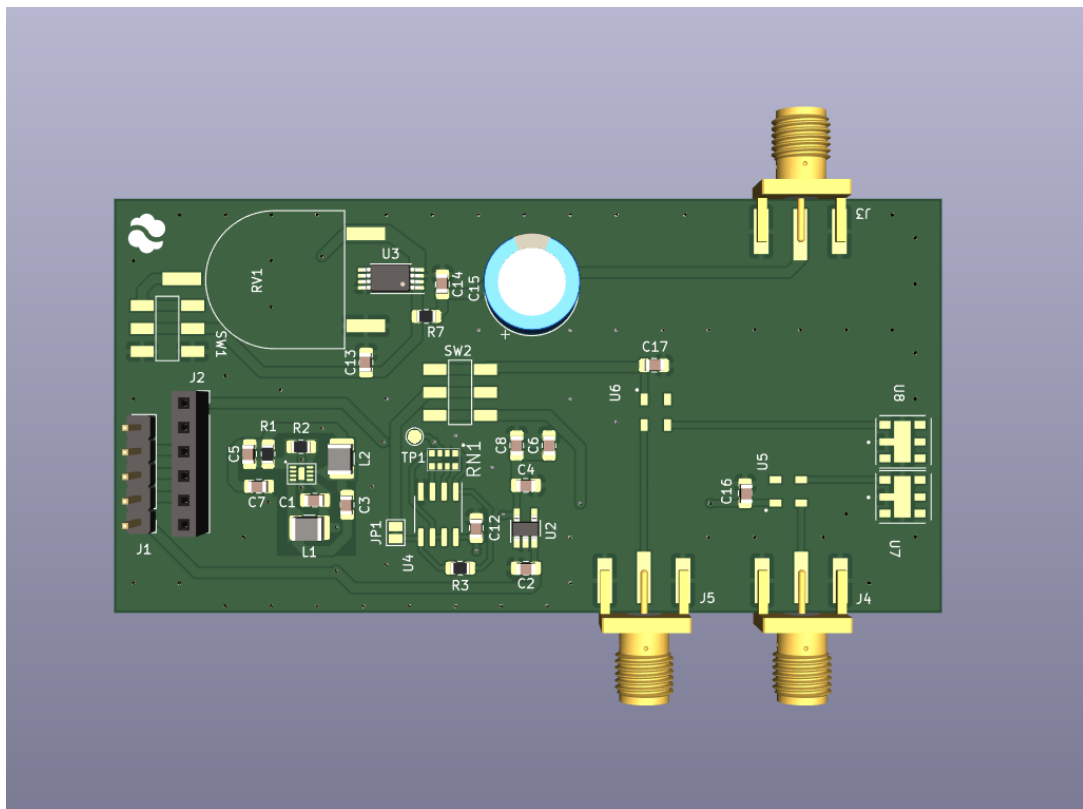


Figure A.1.14: Phase 2 PCB front

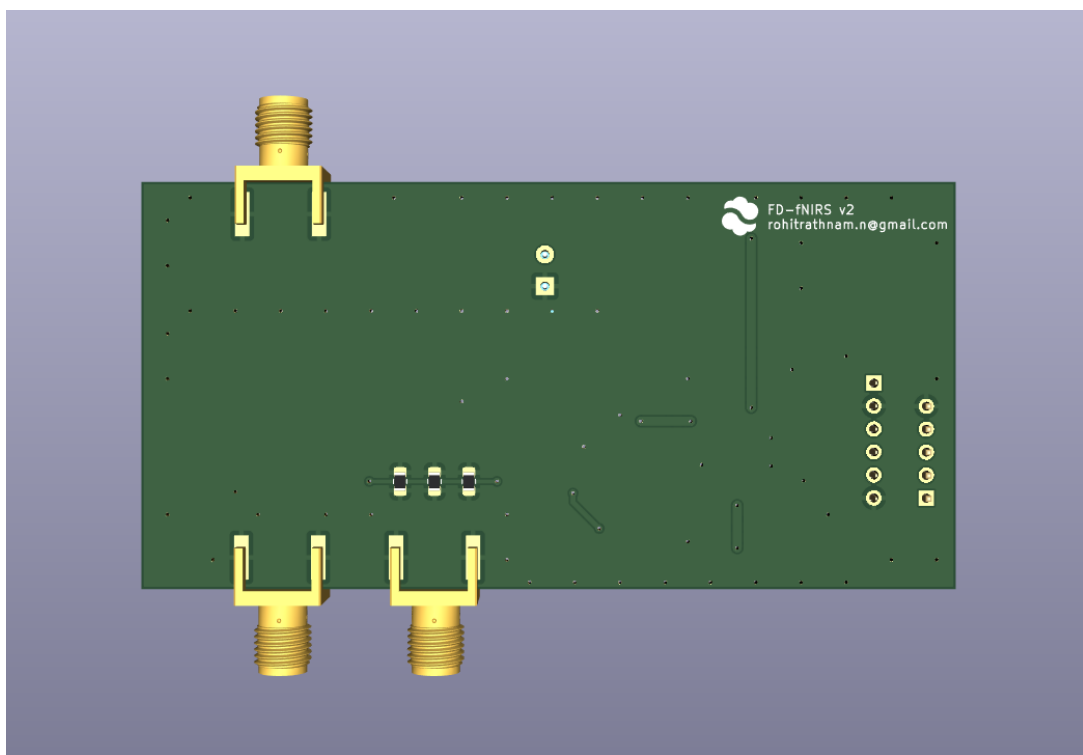


Figure A.1.15: Phase 2 PCB back

Appendix B

Background

B.1 Imaging modalities for neurofeedback training

Different modalities of neuroimaging can be utilised for neurofeedback training, such as EEG, Magneto Encephalography (MEG), Positron Emission Tomography (PET), Single Positron Emission Computed Tomography (SPECT)), Magnetic Resonance Imaging (MRI) and fNIRS [31, 32]. These can often be distinguished on if they provide direct or indirect information about brain activity. MEG and EEG are considered direct methods since they measure the direct result of neuronal activity in the form of electrical or magnetic field in the vicinity. PET, SPECT, MRI, and NIRS are considered indirect methods since they measure haemodynamic changes linked with increased local activity. PET and SPECT monitor the decay of radio isotopes present in the blood as they pass through the brain. In the case of fMRI, it works by detecting changes in deoxyhaemoglobin through its effect on magnetic fields. fNIRS is a diffuse optical imaging method that measures the concentration of oxy and deoxyhaemoglobin in the tissue based on its near infrared absorption properties.

Figure B.1.1 shows a comparison of spatial and temporal sensitivity in different neuroimaging modalities. One can see that MEG and EEG which are also known as Event Related Potentials (ERP), have a high temporal resolution but low spatial sensitivity. In contrast, MRI and PET/SPECT have high spatial sensitivity but lower temporal sensitivity.

Diffuse optical methods including fNIRS offer a good trade-off between spatial and temporal sensitivity. In addition, these systems can be easily adapted into a portable

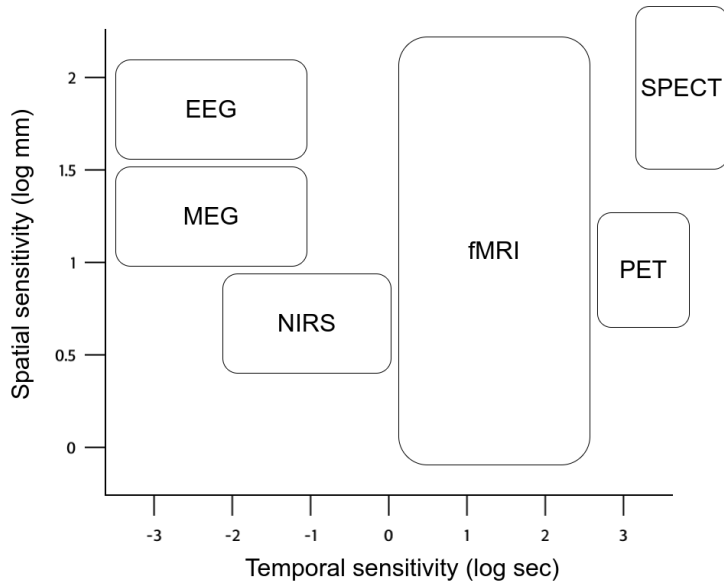


Figure B.1.1: Spatial vs Temporal sensitivity in neuroimaging modalities. Adapted from [32]

wearable form factor, which is not possible for PET or MRI. fNIRS offers benefits in terms of lower cost, ease of use, lower effect of motion on the signal, and few contraindications [6]. These have made it an attractive option for neurofeedback training applications.

B.2 Mechanism of fNIRS

Functional near infrared spectroscopy (fNIRS) is an optical measurement modality that uses light in the near infrared region (600-1000nm). The absorption properties of tissue in these wavelengths is shown in figure B.2.1. The basis for quantitative measurement using fNIRS is the Beer-Lambert law. The law states that the change in light attenuation is proportional to the change in concentration of chromophores, which are colour sensitive particles or functional groups. In this case the chromophores of interest are oxy and deoxyhaemoglobin [33]. The measured changes in haemoglobin levels act as a proxy for neural activity and closes the loop for neurofeedback training. fNIRS offers a way to non-invasively sense brain activity as a wearable device during everyday activities.

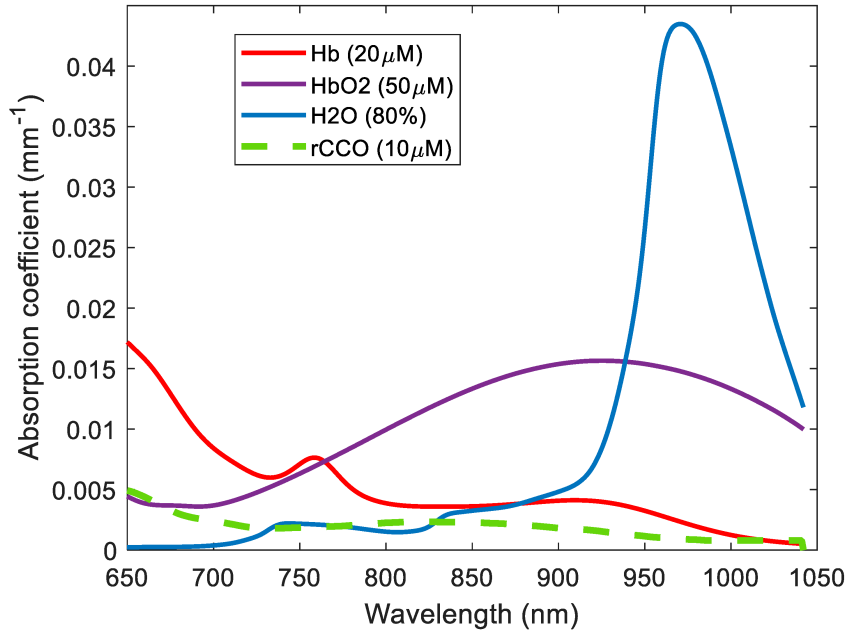


Figure B.2.1: Chromophore absorption coefficients in tissue [34]

B.3 fNIRS techniques

There are three main approaches to fNIRS - continuous wave (CW), frequency domain (FD), and time domain (TD) [8, 35]. The most common modality is CW, where a constant source of light is used, and the intensity of light scattered is measured. This data is used to solve for concentration using the modified Beer-Lambert law. The advantages are that it is simple and cheap to build. However it requires an approximation of a geometry-dependant scattering coefficient μ'_s from lab measured values and therefore is better for relative oxygenation measurements. In the case of time domain methods, short pulses of light are used at the source and the distribution of photon arrival time (shape of received pulse) is measured [36]. This information is used to calculate path length of photons and gives a better measure of the optical properties of the medium [37]. However, the drawback of this method is that it is more complex and expensive to build, especially in terms of high sensitivity needed for the receiver. The frequency domain approach uses modulated light at the source and measures the attenuation and phase shift of the modulated light. This method allows us to calculate the scattering coefficient and therefore absolute oxygenated haemoglobin concentration in the tissue. An added advantage is that the AC amplitude is relatively insensitive to ambient light sources (within the dynamic range of the sensor), reducing the complexity in terms of signal processing [38]. The comparison between fNIRS modalities is summarised in Table B.3.1 For this work, the frequency domain approach

was found to be a good fit for a high accuracy neurofeedback device.

Table B.3.1: Comparison of different fNIRS techniques [8]

Property	Continuous wave	Frequency domain	Time domain
Sampling rate	~100 Hz	~50 Hz	~10 Hz
Penetration depth	Low	Deep	Deep
Differentiate cerebral and extra cerebral tissue	No	Feasible	Feasible
Instrument size	Some small, some bulky	Bulky	Bulky
Instrument stabilisation	No	No	Required
Measurable [Hb] values	Relative	Absolute	Absolute

B.4 Analytical Model

The frequency domain approach involves amplitude modulation of light at a fixed frequency, and the measurement of attenuation and phase of the received signal. Typical modulation frequencies are at the range of 100MHz [38]. For a given sinusoidal light source, the signal can be described as:

$$\text{Signal} = A_{DC} + A_{AC} \times e^{i\Phi} e^{-i\omega t} \quad (\text{B.1})$$

where Φ is phase, ω is the angular frequency, t is time, A_{DC} and A_{AC} represent the respective components. The measurement of interest is the amplitude attenuation ΔA_{AC} and the phase shift $\Delta\Phi$.

Light-tissue interaction for this signal in FD-fNIRS is modelled using the time-dependant form of the standard diffusion equation or radiative transport equation [19]. Applying the diffusion approximation, this is given by:

$$\frac{1}{c} \frac{\partial \phi(r, t)}{\partial t} - D \nabla^2 \phi(r, t) + \mu_a \phi(r, t) = S(r, t) \quad (\text{B.2})$$

where ϕ is the fluence rate, S is the source of photons, c is the speed of light in tissue (refractive index ~ 1.4), where

$$D = \frac{1}{3[\mu_a + \mu_s(1 - g)]} \quad (\text{B.3})$$

and μ_a is the absorption coefficient, μ_s is the scattering coefficient, g is average cosine angle of scattering phase function (anisotropy factor).

Haskell et. al [39] describes different approximations of the diffusion equation based on boundary conditions. In brief, the instrument - tissue geometry can be approximated by a semi-infinite medium with a planar boundary [39]. Thus, the analytical solution to an amplitude modulated point source in a semi-infinite media can be described by B.4 - B.5:

$$\Theta_{lag}(\rho, \omega) = k_{imag}(\omega)r_0 - \arctan\left(\frac{IMAG}{REAL}\right) \quad (B.4)$$

$$A_{att}(\rho, \omega) = \frac{A_{instr}}{4\pi D}(REAL^2 + IMAG^2)^{1/2} \quad (B.5)$$

where

$$REAL = \frac{\exp[-k_{real}(\omega)r_0]}{r_0} - \cos[k_{imag}(\omega)(r_{0b} - r_0)] \frac{\exp[-k_{real}(\omega)r_{0b}]}{r_{0b}} \quad (B.6)$$

$$IMAG = \sin[k_{imag}(\omega)(r_{0b} - r_0)] \frac{\exp[-k_{real}(\omega)r_{0b}]}{r_{0b}} \quad (B.7)$$

$$r_0 = \left[\left(\frac{1}{\mu'_s} \right)^2 + \rho^2 \right]^{1/2} \quad (B.8)$$

$$r_{0b} = \left[\left(\frac{4}{3\mu'_s} \frac{1 + R_{eff}}{1 - R_{eff}} + \frac{1}{\mu'_s} \right)^2 + \rho^2 \right]^{1/2} \quad (B.9)$$

$$k_{real} = \left(\frac{3}{2} \mu_a \mu'_s \right)^{1/2} \left\{ \left[1 + \left(\frac{\omega}{c\mu_a} \right)^2 \right]^{1/2} + 1 \right\}^{1/2} \quad (B.10)$$

$$k_{imag} = \left(\frac{3}{2} \mu_a \mu'_s \right)^{1/2} \left\{ \left[1 + \left(\frac{\omega}{c\mu_a} \right)^2 \right]^{1/2} - 1 \right\}^{1/2} \quad (B.11)$$

where A_{ir} is the amplitude response of the instrument, R_{eff} is the effective reflection for the interface. The approximations made are valid for the conditions $\omega < 1\text{GHz}$ and $\mu'_s \gg \mu_a$. Solving for μ_a and μ'_s , these can be plugged in to the following equation using tabulated molar extinction coefficients for a given wavelength ϵ_λ , for haemoglobin [40].

$$\mu_{a,\lambda} = 2.303\epsilon_\lambda c \quad (B.12)$$

Here c is the required concentration in mol/L [41].